Reijo Pohjonen

Hyperfine Interactions in Superconducting Iron-Chalcogenide and -Pnictide Compounds

Åbo Akademi University

Hyperfine Interactions in Superconducting Iron-Chalcogenide and -Pnictide Compounds

Reijo Pohjonen

Physics
Faculty of Science and Engineering
Åbo Akademi University
Åbo, Finland, 2022

Supervisor Docent Johan Lindén
Faculty of Science and Engineering
Department of Physics
Åbo Akademi University
Finland

Opponent Professor Artur Błachowski
Institute of Physics
Pedagogical University Kraków
Poland

ISBN 978-952-12-4162-8 (PRINT)
ISBN 978-952-12-4163-5 (PDF)

Åbo Akademi
2022

Abstract

This thesis deals with the synthesis and analysis of the hyperfine properties in iron-chalcogenide and -pnictide superconductors as well as related compounds. The experimental studies are based on Mössbauer spectroscopy, X-ray powder diffractometry with Rietveld refinement.

A non-stoichiometric monoclinic Fe_3Se_4 was synthesized. Two iron sites were identified below $T_C \approx 331$ K. The two magnetic sextets exhibits sign of broadening, which could be dealt with either by doubling the number of sextets to four or by introducing a correlated histogram distribution to each sextet. It is inferred that the origin of the distribution is a charge-distribution occurring within each iron site.

An iron chalcogenide sample with nominal composition $FeTe_{0.5}Se_{0.5}$ was synthesized following a solid-state reaction route. Using the field of an 11.7 T magnet textured samples, having the c axes parallel with and normal to the sample surface, were made. Clear indications of vibrational anisotropy, $i.e.$the Goldanskii-Karyagin effect, were observed.

A superconductive $Ba_2Ti_2Fe_2As_4O$ oxypnictide sample was synthesized following a solid-state reaction route. ^{57}Fe Mössbauer spectra indicate that the spin-density wave is suppressed at least down to 77 K. Analysing the temperature-dependent part of the isomer shift, using the Debye model, a Debye temperature of 280-320 K is obtained. This indicates that the local lattice around Fe is rather soft. Fe is formally divalent with a low spin.

A superconductive $BaTh_2Fe_4As_4(N_{0.7}O_{0.3})_2$ oxypnictide sample was synthesized using a high-temperature solid-state reaction route. Fe atoms in $ThFeAsN_{0.7}O_{0.3}$ and $BaFe_2As_2$ and $BaTh_2Fe_4As_4(N_{0.7}O_{0.3})_2$ seem to have practically identical local surroundings $i.e.$ regular or almost regular tetrahedron formed by four As neighbours, that gives rise to almost zero quadrupole splitting. Debye temperature of 352-369 K is obtained. The chemical isomer shift value indicates that Fe is divalent in low-spin state when Th valence is close to +4 and As valence close to -3.

Svensk sammanfattning

Denna avhandling behandlar provsyntes och analys av de hyperfina egenskaperna i järnkalkogenid- och järnpnictidsupraledare såväl som besläktade föreningar. De experimentella studierna bygger på Mössbauerspektroskopi, röntgenpulverdiffraktometri och Rietveldstrukturanalys.

Ett icke-stökiometriskt monoklint Fe_3Se_4 prov syntetiserades. Två järnpositioner identifierades i temperaturer under $T_C \approx 331$ K. De två magnetiska sextetterna i Mössbauerspektret uppvisade tecken på breddning, vilket skulle kunna hanteras antingen genom att fördubbla antalet sextetter till fyra eller genom att införa en korrelerad histogramfördelning för båda sextetterna. Man drog slutsatsen att ursprunget till fördelningen är laddningsfördelningen som förekommer inom varje järnposition.

Ett supraledande järnkalkogenidprov med den nominella stökiometrin $FeTe_{0.5}Se_{0.5}$ syntetiserades med en fastatillståndets reaktionsmetod. Med hjälp av fältet av en 11,7 T magnet orienterades prover med c axeln parallell med provytan eller c axeln vinkelrät mot provytan. Tydliga indikationer på vibrationsanisotropi, dvs Goldanskij-Karyagin-effekten observerades.

Ett supraledande $Ba_2Ti_2Fe_2As_4O$ oxypnictidprov syntetiserades med en fastatillståndets reaktions metod. ^{57}Fe Mössbauerspektra indikerade att eventuella spinndensitetsvågor är dämpade åtminstone ned till 77 K. Analys av den temperaturberoende delen av isomeriförskjutningen med hjälp av Debyemodellen, gav en Debyetemperatur på 280-320 K. Detta indikerar att det lokala gittret runt Fe är ganska mjukt. Järnet är formellt divalent med lågt spinn.

Ett supraledande $BaTh_2Fe_4As_4(N_{0.7}O_{0.3})_2$ oxypnictidprov syntetiserades med en fastatillståndets högtemperaturreaktionsmetod. Fe-atomer i $ThFeAsN_{0.7}O_{0.3}$ och $BaFe_2As_2$ och $BaTh_2Fe_4As_4(N_{0.7}$-$O_{0.3})_2$ verkar ha praktiskt taget identiska lokala omgivningar dvs regelbundna eller nästan regelbundna tetraedrar av fyra arsenikgrannar, vilket ger upphov till en väldigt liten kvadrupolspjälking. Debyetemperaturer av 352-369 K erhölls. Den kemiska isomeriförskjutningen indikerar att Fe är tvåvärt i ett lågspinntillstånd då Th-valensen är nära +4 och As-valensen nära -3.

Acknowledgments

This research work has been carried out in collaboration with the Mössbauer research group at Åbo Akademi University Faculty of Science and Engineering, Department of Chemistry at Aalto University, and Department of Physics, Zhejiang University in Hangzhou, China.

I would like to thank Professor Ronald Österbacka for allowing me to complete my doctoral thesis at Åbo Akademi. Above all, I would like to thank my supervisor, Docent Johan Lindén, for his valuable work in guiding me to experimental work and writing articles. I also want to express my gratitude to my colleague Mr. Fredrik Lindroos for helping me in all areas in physics to return to research after so many decades. I would also want to thank Dr. Kjell-Mikael Källman for his help with the technical issues.
Finally, I would like to sincerely thank my beloved wife, Liisa, who has endured for years with great patience the many evenings and weekends I have focused exclusively on doing my research.

Reijo Pohjonen

LIST OF THE INCLUDED ARTICLES AND THE AUTHOR'S CONTRIBUTION

This thesis consists of an introductory part and four original refereed articles in scientific journals.

I **R. Pohjonen, O. Mustonen, M. Karppinen and J. Lindén**, Mössbauer study of magnetism in Fe_3Se_4, Journal of Alloys and Compounds 746 (2018) 135-139.

II **R. Pohjonen, F. Lindroos, G.C. Tewari and J. Lindén**, Investigating the vibrational lattice anisotropy in $FeTe_{0.5}Se_{0.5}$ using magnetically oriented crystallites, Solid State Communications 312 (2020) 113877.

III **R. Pohjonen, J. Lindén, Shi-Huai Sun and Guang-Han Cao**, Mössbauer study of $Ba_2Ti_2Fe_2As_4O$, Journal of Alloys and Compounds 848 (2020) 155706.

IV **R. Pohjonen, J. Lindén, Bai-Zhuo Li and Guang-Han Cao**, ^{57}Fe Mössbauer study of $BaTh_2Fe_4As_4(N_{0.7}O_{0.3})_2$, Phys. Status Solidi B (2021) 2100125.

Author's contribution

Paper I

The idea for this work came from J. Lindén. X-ray diffraction and Rietveld analysis was made by O. Mustonen. The author did the sample synthesis and Mössbauer measurements and participated analysing all the data. The author wrote the paper together with the co-authors.

Paper II

The idea for this work came from J. Lindén. X-ray diffraction was done by G.C. Tewari. The author together with F. Lindroos prepared the graphics presented. All other experimental work was planned and executed by the author. The manuscript was written by the author and finalized together with the co-authors.

Paper III

The author did all the experiments presented in this paper except the synthesis of the sample, which was done at Zhejiang University, Hangzhou, China. The author analysed all the data and wrote the manuscript and finalized the paper together with the co-authors.

Paper IV

The synthesized sample was obtained from Zhejiang University, Hangzhou, China. The author carried out the Mössbauer measurements, analysed all the data with supervisor, wrote the manuscript and participated in the finalizing of the paper with the co-authors.

LIST OF ADDITIONAL ARTICLES

1. **A. Sklyarova, S. Shinoda, T. Nagumo, V. I. Chizhik, V. V. Matveev, J. Lindén, R. Pohjonen, T. Suzuki, T. Nakayma, H. Suematsu**, Effect of Blocking and Superconducting Layer Doping on the Superconductivity and Magnetic Properties of Polycrystalline $Sr_2CaCu_2O_6$, Journal of Superconductivity and Novel Magnetism 31 (2018) 2711-2717.

2. **Girish C. Tewari, Divya Srivastava, Reijo Pohjonen, Otto Mustonen, Antti J. Karttunen, Johan Lindén and Maarit Karppinen**, Fe_3Se_4: A Possible Ferrimagnetic Half-Metal?, Journal of Physics: Condensed Matter, 32 (2020) 455801.

α, β, γ	Lattice angles
δ_0	Chemical Isomer Shift
δ_{SOD}	Second-order Doppler Shift
ΔE_Q	Quadrupole splitting
η	Asymmetry parameter of EFG
γ	Gamma quantum
Γ	The Heisenberg natural line width
θ_{D}	Debye temperature
μ	The magnetic dipole moment
σ_a	Nuclear cross section of absorption
χ^2	Parameter describing goodness of fit
a, b, c	Lattice parameters
B	Magnetic hyperfine field
$\langle B \rangle$	Average hyperfine magnetic field
B_{eff}	Effective magnetic field
eQ	Quadrupole moment
eQV_{zz}	Quadrupole coupling constant
EFG	Electric Field Gradient
FC	Field Cooling
f_a	Recoilfree fraction of absorption
GKE	Goldanskii-Karyagin Effect
H_{c}	Coercivity field
h	Planck's constant
$\hbar$	Dirac's constant (Planck's constant h divided by 2π)
IS	Isomer Shift
I	Nuclear spin quantum number
k_{B}	Boltzmann's constant
m_I	Nuclear magnetic spin quantum number
n_a	Number of Mössbauer nuclei per square centimeter
RT	Room Temperature
S	Electronic spin
SDW	Spin Density Wave
t_a	Absorber thickness in cm
T	Effective absorber thickness
T_c	Critical temperature of magnetic transition
T_{C}	Curie temperature
$\langle u^2 \rangle$	Mean square displacement value
V_{zz}	The main component of the electric field gradient
V	The electric potential
XRD	X-Ray Diffractometry
ZFC	Zero-Field Cooling

PART I: OVERVIEW OF THE THESIS

CHAPTER I

Introduction

1.1 Short review

Since the first paper reporting iron-based superconductivity with $T_c = 26$ K in $LaFeAsO_{1-x}F_x$, (2008) [58] several tens of superconducting layered iron pnictides and chalcogenides have been reported. These materials contain a common building block of a square lattice of Fe^{2+} ions with tetrahedral coordination with pnictogen (P and/or As) or chalcogen ions. It was widely believed that elements with a large magnetic moment were harmful for the emergence of superconductivity because the magnetism arising from the static ordering of magnetic moments competes with superconductivity [64, 65]. Iron-based superconductive pnictide and chalcogenide phases can be studied using ^{57}Fe Mössbauer spectroscopy. ^{57}Fe is the most frequently used nucleus for Mössbauer spectroscopy measurements. This method gives information on the hyperfine interactions between the ^{57}Fe nuclei and the surrounding structure and from these interactions certain material parameters concerning valences, charges and magnetic properties are obtained. Also the relativistic contribution to the experimentally observed isomer shift, second-order Doppler shift (SOD), due to the thermal motion of the emitting and absorbing nuclei is obtained. Under favourable conditions they could shed light on the mechanism of superconductivity in these phases. Almost all parent phases of Fe-based superconductors are semimetals with an antiferromagnetic ground state so it is possible to make comparison between the various phases and see whether the obtained parameters correlate with the superconductive properties.

1.2 Objectives

The aim of this work is to study the hyperfine interactions in superconducting iron-chalcogenide, iron-pnictide and related compounds at temperatures below and above superconductivity transition temperature, and to study the evolution of isomer shift, quadrupole splitting and the magnetic properties in all temperature ranges. Compounds of $FeTe_{0.5}Se_{0.5}$, $Ba_2Ti_2Fe_2As_4O$ and $Ba_2Ti_2Fe_2As_4O$ belonging to groups 122, 22241 and 12442 were synthesized and the properties were studied. Additionally the non-superconducting compound Fe_3Se_4 was synthesized and its properties studied. As ^{57}Fe Mössbauer spectroscopy is very sensitive for detection the appearance and vanishing of magnetic ordering, the method was a good choice for this study. The description of the synthesis process, phase purity, superconductivity and magnetic properties are presented in this thesis.

1.3 Summary of publications

This thesis is based on the following original publications:

I. R. Pohjonen, O. Mustonen, M. Karppinen and J. Lindén,
Mössbauer study of magnetism in Fe_3Se_4, Journal of Alloys and Compounds 746 (2018) 135-139.

A non-stoichiometric monoclinic Fe_3Se_4 sample was successfully synthesized and studied by ^{57}Fe Mössbauer spectroscopy at various temperatures. Below $T_C \approx 331$ K two iron sides were readily identified from the two magnetic sextets. The internal fields for the iron atoms are low. Both sextets exhibits sign of broadening. We introduced a correlated histogram charge-splitting to each sextet. Using this method the hyperfine parameter sets for each component were obtained from two distributions, the spectra were analysed assuming the presence of a modulation of the iron valence. It is inferred that the origin of the distribution is a charge-splitting occurring within each iron side.

II. R. Pohjonen, F. Lindroos, G.C. Tewari and J. Lindén,
Investigating the vibrational lattice anisotropy in $FeTe_{0.5}Se_{0.5}$ using magnetically oriented crystallites, Solid State Communications 312 (2020) 113877.

An iron chalcogenide sample with the nominal composition $FeTe_{0.5}Se_{0.5}$ was synthesized following a ceramic method. X-ray diffraction followed by Rietveld analysis were used for verifying the phase content. Using the field of an 11.7 T NMR magnet, textured samples having the c axes parallel with and normal to the sample surface, were made. ^{57}Fe Mössbauer spectroscopy in transmission geometry was used for characterizing the hyperfine parameters of the iron site. Clear indications of vibrational anisotropy, i.e. the Goldanskii-Karyagin effect, were observed. Fitting spectral absorption with the Debye model yielded rather low Debye temperatures of $255(3)$ and $303(3)$ K, for samples texturized with the c axis parallel with and perpendicular to the Mössbauer γ beam, respectively. Also the second-order Doppler shift of the isomer shift data exhibited a similar, although weaker, anisotropy.

III. R. Pohjonen, J. Lindén, Shi-Huai Sun and Guang-Han Cao,
Mössbauer study of $Ba_2Ti_2Fe_2As_4O$, Journal of Alloys and Compounds 848 (2020) 155706.

A superconductive $Ba_2Ti_2Fe_2As_4O$ oxypnictide sample was synthesized following a conventional solid-state reaction route. The crystal structure of $Ba_2Ti_2Fe_2As_4O$ can be viewed as an intergrowth of $BaFe_2As_2$ and $BaTi_2As_2O$ containing superconducting $[Fe_2As_2]$ layers and conducting $[Ti_2O]$ sheets. $Ba_2Ti_2Fe_2As_4O$ is paramagnetic at least down to 77 K in contrast to the $BaFe_2As_2$ parent phase, which exhibits a spin-density order below ~ 140 K. Using the Debye model, for analyzing the temperature-dependent part of the isomer shift data and the sample absorption for $Ba_2Ti_2Fe_2As_4O$, rather low Debye temperatures of 280-320 K was obtained indicating that the local lattice around Fe is formally divalent with low spin.

IV. R. Pohjonen, J. Lindén, Bai-Zhuo Li and Guang-Han Cao,
Mössbauer study of $BaTh_2Fe_4As_4(N_{0.7}O_{0.3})_2$, Phys. Status Solidi B (2021), 2100125

A superconductive $BaTh_2Fe_4As_4(N_{0.7}O_{0.3})_2$ oxypnictide sample was synthesized using a high-temperature solid-state reaction route. X-ray followed by Rietveld analysis was used for checking the phase content. ^{57}Fe Mössbauer spectroscopy in transmission geometry was used for characterizing the hyperfine parameters of the iron site. Owing to the slightly deformed tetrahedral As coordination

around Fe, the quadrupole coupling constant of Fe is non-zero, but small. This is visible in particular below 80 K. Judging by the consistency two Debye temperatures of 352 K and 369 K values obtained using the total absorption and the second-order Doppler shift, a harmonic approximation for the phonon spectra can be assumed.

CHAPTER II

^{57}Fe Mössbauer spectroscopy

2.1 Mössbauer effect

The Mössbauer effect or recoilless nuclear resonance fluorescence is the recoil-free emission and absorption of gamma rays. This physical phenomenon was discovered by Rudolf Mössbauer in 1958, and 1961 Professor Mössbauer was awarded the Nobel prize in physics for his discovery. The Mössbauer effect involves the resonant and recoil-free emission and absorption of gamma radiation by atomic nuclei bound in a solid lattice. When a γ quantum is emitted there is a non-zero probability that a phonon is also created and the emission is not recoilless. The recoilless absorption in the Mössbauer effect is more likely at low temperatures. The probability for phonon creation grows with the energy of the γ quantum. This restrict the energy of the recoilless γ transition to the order of 10-120 keV.

2.2 Mössbauer spectroscopy

Mössbauer spectroscopy measures the spectrum of energies at which specific nuclei resonantly absorb γ rays. For one nucleus to emit a γ quantum and a second to absorb it efficiently, the atoms containing the two nuclei must be bonded chemically in solids, $i.e.$ gaseous or liquid states do not work. Mössbauer spectroscopy is based on the Mössbauer effect and a simple Doppler modulation of recoillessly emitted γ quanta. Mössbauer spectroscopy, or resonant gamma-ray emission/absorption spectroscopy, is the study of the interaction of electromagnetic radiation in the energy range from 10^4 to 10^5 eV with atomic nuclei. The nuclear transition lifetime is linked to nuclear energy uncertainty by the Heisenberg uncertainty relation, such that

$$\Delta E \Delta t \geq \hbar, \tag{2.1}$$

where ΔE and Δt are the uncertainties in energy and time and $\hbar$ is Planck‘s constant h divided by 2π. This relationship results in a distribution of energies for a nuclear transition that follows a Breit-Wigner, or Lorentzian distribution centered at the mean energy E_0 for thin absorbers.

The emission-absorption resonance intensity depends on

- the nuclear properties,
- the source properties and on
- the absorber properties.

The nuclear properties contain the cross-section of γ-ray absorption and hence E_γ, I_g and I_e (nuclear spin quantum numbers of ground (g) and excited (e) state) and α the natural abundance of the resonant nuclide. The source properties are the recoil-free fraction f_s and the source line width Γ_s and the absorber properties include the recoil-free fraction for absorption f_a and the absorber line width Γ_a.

Resonance absorption is observable only if the emission and absorption lines overlap sufficiently. Perfect overlap can be restored by making use of the Doppler effect. Lines must not to be too narrow or too broad when the emission line is shifted by Doppler modulation velocities. Eq. 2.1 can also be written as

natural line width Γ

$$\Gamma = \frac{\hbar}{\tau} \tag{2.2}$$

where Γ is the width of the γ-ray energy distribution at the half height and τ the mean life time of the excited state of the nuclei. For the source and absorber Γ_a, $\Gamma_s > \Gamma$.
By far the most common isotope studied using Mössbauer spectroscopy is ^{57}Fe ($E_\gamma = 14.4$ keV) with $t_{\frac{1}{2}} = 99.3$ ns [13].

2.3 Mössbauer measurements

In Mössbauer spectroscopy the transition energies between allowed transitions of certain nuclei are measured. This can be achieved using a Mössbauer spectrometer, Fig. 3.1, where the ^{57}Co source decaying through electron capture to ^{57}Fe and producing the 14.4 keV γ quanta is fixed to the drive coil. The emitted γ quanta are received by the sample (absorber) through a collimator. Transmitted γ quanta are detected using a proportional counter (detector). With a cryostat and a temperature control unit the temperature of the sample can be regulated. For measurements at higher temperatures the sample can be placed in a special oven. Owing to the cylindrical geometry, in the other end of the drive unit a second sample can be placed (e.g. an α-iron calibration foil and after the velocity calibration some other sample), thus two simultaneous Mössbauer measurements are possible. From the pre-amplifier the signal is led to the amplifier and further to the single-channel analyzer and further to the multi-channel analyzer (MCA) which receives also the velocity (mm/s) signal coming from the drive unit and creates the final output data.

In Mössbauer transmission experiment the radioactive source is periodically moved with controlled velocities, Doppler velocities, +v and -v away/towards from the absorber. The motion modulates the energy of the γ -photons arriving at the absorber because of the
Doppler effect

$$E_\gamma = E_0 \left(1 \pm \frac{|v|}{c}\right) \tag{2.3}$$

where E_γ is the energy of the emitted γ-ray, E_0=14.4 keV (commonly studied isotope ^{57}Fe), v is the Doppler velocity in mm/s and c is the velocity of light.

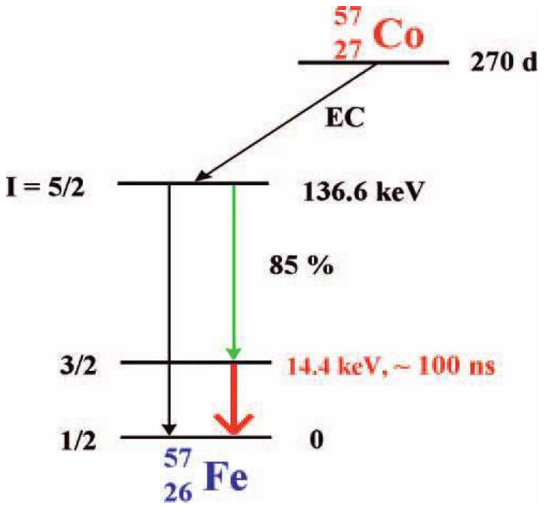

Figure 2.1: Decay scheme of ^{57}Co producing ^{57}Fe.

2.3.1 Hyperfine interactions

There are two types: magnetic and electric hyperfine interaction. For both type of interactions the nuclear spins couple with the external fields wich cause splitting of the resonance lines. The magnetic interaction gives local information on the magnetic order (disorder) and the electric interactions gives local information about valences and lattice symmetries. There are three types of nuclear interactions that are observed in a Mössbauer spectra

(i) Electric monopole interaction
occurs between protons of the nucleus and electrons (mainly s-electrons) penetrating the nucleus. The observable Mössbauer parameter is the isomer shift δ_0 (mm/s), which can shift the spectrum to higher or lower energies. Isomer shift originates from the Coulomb interaction between the nuclear charge distribution over the radius of the nucleus in its ground and excited state, and the electron charge density at the nucleus. The isomer shift depends most strongly on the valence- and spin states of the Fe atom, as shielding effects due to valence electrons will influence the s-electron density at the nucleus [25],

$$\delta_0 = C\frac{\delta R}{R}\left(|\Psi_A(0)|^2 - |\Psi_S(0)|^2\right) \tag{2.4}$$

where C is a constant for a specific isotope, $\frac{\delta R}{R}$ the relative change in the radius of the nucleus between the excited state and ground state and $|\Psi_A(0)|^2$ and $|\Psi_S(0)|^2$ are the electronic charge densities in the core of the absorber and source. $|\Psi_A(0)|^2$ and $|\Psi_S(0)|^2$ mainly originates from the ability of $1s$ and $2s$ core-shell electrons to penetrate the nucleus. Valence orbitals of p-, d- or f-character having nodes at $r = 0$ cannot contribute to $|\Psi(0)|^2$ except for minor relativistic contributions of p- electrons.
The isomer shift (δ_0) is useful for determining oxidation state, spin state (HS, IS and LS) and the electro-negativity of ligands. High spin (HS) complexes are coordination complexes containing

unpaired electrons at all energy levels, they are paramagnetic complexes and can be attracted to an external magnetic field. Low spin (LS) complexes are coordination complexes containing paired electrons at low energy levels. According to the Hund's rule all orbitals must be occupied before pairing begins, this situation only occurs when the pairing energy is greater than the crystal field energy.

The experimentally observed isomer shift, δ_{exp}, includes a temperature dependent non-zero, relativistic contribution which is called second-order Doppler shift, δ_{SOD} [59] so that

$$\delta_{\mathrm{exp}} = \delta_0 + \delta_{\mathrm{SOD}}, \tag{2.5}$$

where δ_0 is the true isomer shift.

When the emitting or absorbing atom is thermally vibrating with mean squared velocity $\langle v^2 \rangle$, the second-order Doppler shift is given by

$$\delta_{\mathrm{SOD}} = -E_\gamma \frac{\langle v^2 \rangle}{2c^2}. \tag{2.6}$$

The value of δ_{SOD} drops with temperature and becomes small, although non-zero, at liquid helium temperature, as $\langle v^2 \rangle$ is proportional to the mean kinetic energy (including zero-point motion) of the Mössbauer atom.

Using the Debye model the second-order Doppler shift (SOD) can be expressed as [38]

$$\delta(T) = \delta_0 - \frac{9k_{\mathrm{B}}\theta_{\mathrm{D}}}{16M_{\mathrm{eff}}c} - \frac{9k_{\mathrm{B}}T}{2M_{\mathrm{eff}}cx_{\mathrm{D}}^3}\int_0^{x_{\mathrm{D}}} \frac{x^3 dx}{e^x - 1} \tag{2.7}$$

where M_{eff} is the effective mass of the vibrating atom, θ_D the Debye temperature, k_{B} Boltzmann's constant and and $x_{\mathrm{D}} = \frac{\theta_{\mathrm{D}}}{T}$.

The Debye temperature θ_D is given as [60]

$$\theta_D = \frac{\hbar\omega_D}{k_{\mathrm{B}}} \tag{2.8}$$

where ω_D is Debye frequency (a measure of strength of the bonds between Mössbauer atom and the lattice) and k_B Boltzmann's constant.

(ii) Electric quadrupole interaction
between the electric quadrupole moment of an ellipsoidal nuclear charge distribution and the electric field gradient (EFG) of a non-spherically symmetric charge distribution splits the degeneracy of the excited state into two lewels that are separated by the quadrupole splitting (energy difference) ΔE_Q.

EFG is obtained as the sum of the principal tensor components of the Laplace equation, $\nabla^2 V = 0$ or $V_{zz} + V_{xx} + V_{yy} = 0$ and the coordinate system chosen so that $|V_{zz}| \geq |V_{yy}| \geq |V_{xx}|$.

The EFG at the nucleus will split the ^{57}Fe excited nuclear $I = \frac{3}{2}$ state into two levels: $|I_z\rangle = \pm\frac{1}{2}$ and $\pm\frac{3}{2}$ and the ^{57}Fe Mössbauer spectrum becomes a doublet.
Quadrupole splitting is measured as the separation (mm/s) between these doublet peaks and reflects

the character of the electric field at the nucleus.
The energy difference between the resonance lines of intensities in a quadrupole doublet is

$$\Delta E_Q = \frac{eQV_{zz}}{2}\left(1+\frac{\eta^2}{3}\right)^{\frac{1}{2}} \tag{2.9}$$

where Q is the nuclear quadrupole moment of ^{57}Fe isotope, eQV_{zz} the nuclear quadrupole coupling constant and η the unitless asymmetry parameter defined as [62]

$$\eta = \frac{|V_{xx}-V_{yy}|}{|V_{zz}|} \tag{2.10}$$

Due to the choice of coordinate system $0 \leq \eta \leq 1$.
The quadrupole splitting can be used for determining oxidation state of Fe, site symmetry and the arrangement of ligands surrounding the Fe atom.

The energy eigenvalues for electric quadrupole interaction ^{57}Fe is given as [56], an approximation but a very good one

$$E = \frac{eQV_{zz}}{4I(2I-1)}\left[3m_I^2 - I(I+1)\right]\left(1+\frac{\eta^2}{3}\right)^{\frac{1}{2}} \tag{2.11}$$

where m_I is the z-component of the nuclear spin quantum number I.
We did not use approximation, but a direct diagonalization of the Hamilton function made by our fitting program. The approximation can be good to illustrate the transitions though.

(iii) Magnetic hyperfine interaction (the nuclear Zeeman effect).
When a material is magnetically ordered, $i.e.$ it has electronic spin S with a specific value and direction, the nucleus will see a non-zero magnetic field B. This gives rise to an interaction between the nuclear magnetic dipole moment (μ) and an applied or atomic magnetic field at the nucleus. That occurs when the nucleus is in a state with nuclear spin quantum number $I > 0$. The nuclear Zeeman effect will split the state with spin quantum number I into $2I+1$ equally spaced and non-degenerate substates characterized by the sign and magnitude of the nuclear magnetic spin quantum number m_I.

Energy eigenvalues for magnetic interactions ^{57}Fe are [57]

$$E = -g\mu_N B m_I \tag{2.12}$$

where g is the nuclear g-factor and μ_N the nuclear Bohr magneton.

When magnetic and electric quadrupole interaction is combined i.e. when both interactions are present we get the eigenvalues [61]

$$E = -g\mu_N B m_I + \frac{eQV_{zz}}{4I(2I-1)}\left[3m_I^2 - I(I+1)\right]\left(1+\frac{\eta^2}{3}\right)^{\frac{1}{2}} \tag{2.13}$$

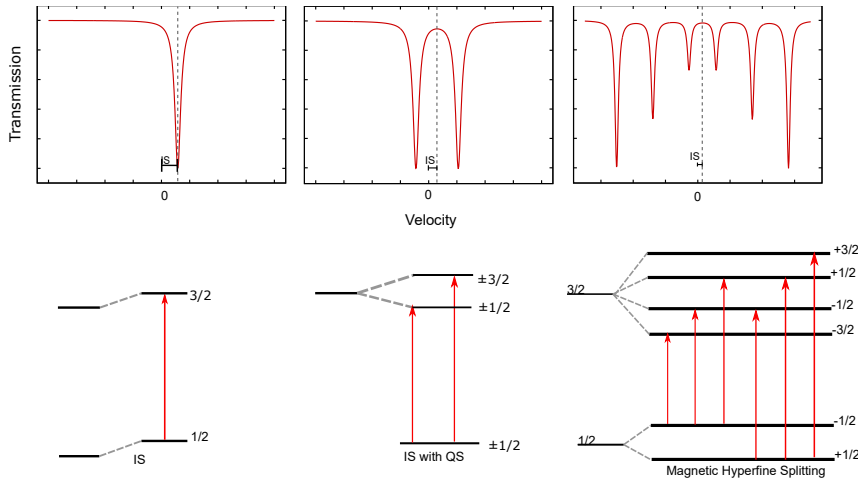

Figure 2.2: Hyperfine splitting of ^{57}Fe nuclear levels

2.3.2 Recoilfree fraction f_a of absorption

The temperature dependence of of the recoil-free fraction $f(T)$ is given by [55]

$$f(T) = \exp\left[-\langle x^2\rangle \frac{E_\gamma^2}{(\hbar c)^2}\right] \tag{2.14}$$

where $\langle x^2\rangle$ is the mean square displacement. Both quantities $\langle x^2\rangle$ and $\langle v^2\rangle$ can be derived from the Debye model for the energy distribution of phonons in a solid, leading to the following expression

$$f_{\mathrm{a}} = \exp\left[-\frac{6E_R}{k_{\mathrm{B}}\theta_{\mathrm{D}}}\left(\frac{1}{4} + x_{\mathrm{D}}^{-2}\int_0^{x_{\mathrm{D}}} \frac{x\,dx}{e^x - 1}\right)\right] \tag{2.15}$$

where E_R is the recoil energy. Recoilfree fraction f_a of absorption determines the absorption i.e. the line intensity.

2.4 Anisotropy in the crystal

If the bonding forces on a Mössbauer nucleus in a crystal do not have cubic symmetry, the amplitudes of the atomic oscillations $\langle x^2\rangle$ (the mean square vibrational displacement) in various directions are not the same, this will lead in an anisotropic behaviour of the recoil-free fraction f_a.
The angular dependence of the quadrupole interaction is reflected in the relative line intensities $I_{\frac{3}{2}}(\theta)$ and $I_{\frac{1}{2}}(\theta)$, corresponding to the transitions $\Delta m = \pm 1$ and 0, respectively. This, as a result, leads to the relative absorption intensities in the subspectra split by hyperfine interactions having a different ratio of the line intensities vs. the angle θ between the γ-ray propagation direction and the principal axis of the electric field gradient V_{zz}. This can be written as [21]

$$\frac{I_{\frac{3}{2}}(\theta)}{I_{\frac{1}{2}}(\theta)} = \frac{1+\cos^2\theta}{\frac{2}{3}+\sin^2\theta} \tag{2.16}$$

For a powder absorber one should integrate the equation over a full solid angle 4π which leads to

$$\frac{\int_0^\pi I_{\frac{3}{2}}(\theta)\sin\theta d\theta}{\int_0^\pi I\frac{1}{2}(\theta)\sin\theta d\theta} = 1. \tag{2.17}$$

For a polycrystalline sample when the recoilless radiation is anisotropic and the recoilfree fraction f_a itself is a function of θ, the integration of Eq. 2.16 over the space angle 4π weighting with $f_a(\theta)$ leads to:

$$\frac{\int_0^\pi (1+\cos^2\theta) f_a(\theta)\sin\theta d\theta}{\int_0^\pi (\frac{2}{3}+\sin^2\theta) f_a(\theta)\sin\theta d\theta} = F[f_a(\theta)] \neq 1. \tag{2.18}$$

When f_a is a constant Eq. 2.17 will follow.

This was first experimentally observed by Goldanskii [19] in polycrystalline samples and explained theoretically by Karyagin [23]. Hence this phenomenon is known as the Goldanskii-Karyagin effect. For polycrystalline samples there are several possible explanations for asymmetries of Mössbauer doublets; preferred orientation of the crystallites in the prepared absorber (texture effects), the Goldanskii-Karyagin effect, impurities or simply a natural feature due to the properties of the crystal structure [24]. In Mössbauer spectroscopy the texture is reflected in the intensities of the Mössbauer spectrum. Due to texturizing the quadrupole-split doublet of the Mössbauer spectra have a characteristic asymmetry, which can be removed by turning the sample into the so called magic angle ($\theta \approx 54.7°$) with respect to the direction of the incoming Mössbauer γ-ray beam. In Eq. 2.16 the ratio $\frac{I_{\frac{3}{2}}(\theta)}{I_{\frac{1}{2}}(\theta)}$ becomes 1 when $\theta \approx 54.7°$. Sometimes powdered crystallites can be oriented (intentionally texturized) using an external magnetic field and fixed in the desired direction by letting a mixture of powder and a bonding agent harden in the field. In order for this to work the magnetic susceptibility must exhibit an anisotropy along the crystalline directions. The method has been used *e.g.* for high-T_c cuprate superconductors [28].

CHAPTER III

Experimental details

3.1 Synthesis of materials

Synthesis of materials requires an understanding of the principles of crystal chemistry, phase equilibria, thermodynamics and reaction kinetics [3]. Depending on how successfully the synthesis is performed, the crystal structure with desired properties are obtained and impurity phases are avoided. The factors on which the feasibility and rate of a solid state reaction depend include, reaction conditions, structural properties of the reactants, surface area of the solids, their reactivity and the thermodynamic free energy change associated with the reaction.[66]
The importance of grinding and mixing well the starting materials, to maximize the reagents surface area, cannot be overemphasized.

The ceramic method is most commonly employed to prepare solid materials. The procedure involves several minutes of either manual or mechanical grinding of the starting materials containing the relevant metals and heating them at high temperatures with intermediate grinding when necessary. The ceramic method suffers from several disadvantages. Solids do not react at room temperature over normal time scales and it is necessary to heat them to much higher temperatures, often from 1000 to $1500\,^{\circ}\mathrm{C}$ in order for the reaction to occur at an appreciable rate. When no melt is formed during the reaction, the entire reaction must occur in the solid state, initially by a phase boundary at the points of contact between the components and later by diffusion of the constituents through the product phase. In our polycrystalline mixture of reactants, the individual particles were ground with an agate pestle and mortar to approximately 10 μm in size, which represents diffusion volumes of roughly 10000 unit cells. As the reaction progresses, diffusion paths keep becoming longer and the reaction rate slower. The product interface between the reacting particles acts as a barrier. The reaction can be sped up to some extent by intermittent grinding and pelletizing (to encourage intimate contact between crystallites) between heating cycles. There is no simple way of monitoring the progress of the reaction in the ceramic method. Even in successfully synthesized samples small defects and traces of impurity phases can be observed, the presence of which influence on the physical properties of these samples. Appropriate conditions that lead to the completion of the reaction can be decided only by trial and error.
For safety the mixing and grinding of the powders should take place in an inert gas atmosphere because many of the chalgogenide and pnictide elements are toxic and sensitive to oxidation.

During this work polycrystalline samples were synthesized following high-temperature conventional solid-state reaction schemes.

3.2 Sample preparations

Fe_3Se_4 (Paper I).
For the investigation of a slightly non-stoichiometric ferrimagnetic iron chalcogenide compound Fe_3Se_4 we chose the selenium content of 56.1 at.% based on the phase diagram in [1]. Stoichiometric ratios of powder Fe and ground shots of Se were mixed, pressed into a pellet at 10 kbar, sealed in a vacuum quartz ampoule, slowly heated up to 750 °C and annealed for 48 h. The resulting powder was reground, pressed into a pellet at 10 kbar, again sealed in a vacuum quartz ampoule and annealed in furnace at 400 °C for 18 h and slowly cooled to room temperature.

$FeTe_{0.5}Se_{0.5}$ (Paper II).
For $FeTe_{0.5}Se_{0.5}$ polycrystalline sample stoichiometric mixtures of iron, tellurium and selenium powders were sealed into a quartz tube under vacuum and slowly heated from room temperature to 680 °C and sintered at this temperature for 24 h. Then the ampoule was quickly removed from the furnace and quenched into cold water and the resulting sample powder was reground, pressed into pellets at 10 kbar, again sealed in an evacuated quartz tube, annealed for 24 h at 680 °C and quenched in cold water. Quenchings were performed to see if phases of lower symmetry would appear as was the case in $Fe_{1-x}Se_x$ [31].

$Ba_2Ti_2Fe_2As_4O$ (Paper III).
The polycrystalline oxypnictide sample $Ba_2Ti_2Fe_2As_4O$ was synthesized at Zhejiang University in China [40] using high-purity starting materials barium, titanium, iron, arsenic and titanium dioxide. A stoichiometric mixture of materials was placed into an alumina tube and sealed in evacuated quartz ampoule and slowly heated to 1173 K and annealed for 24 h. Then the product was ground, pelletized and sintered at 1373 K in evacuated quartz ampoule for 40 h and cooled in furnace to room temperature. This was named Sample 1. Some of this as prepared sample was annealed at 773 K for 40 h in a vacuum. This was named Sample 2.

$BaTh_2Fe_4As_4(N_{0.7}O_{0.3})_2$ (Paper IV).
The polycrystalline $BaTh_2Fe_4As_4(N_{0.7}O_{0.3})_2$ sample was synthesized at Zhejiang University in China [46] by a high-temperature solid-state reaction method using the source materials Ba rods, Fe powders, As pieces and ThO_2 powders. First the intermediate materials Th, Th_3N_4, Th_3As_4, FeAs, and $BaFe_2As_2$ were prepared. Fe_2As and Th_3As_4 were prepared by heating their stoichiometric mixtures in sealed evacuated quartz ampoule to 1123 K, holding for 30 h. $BaFe_2As_2$ was prepared by reacting the mixtures of BaAs and Fe_2As at 1273 K for 40 h. Other intermediate materials Th, Th_3As_4 and FeAs were prepared as reported elsewhere [43]. Then, stoichiometric mixtures of Fe, ThO_2, Th_3As_4, Th_3N_4 and FeAs and $BaFe_2As_2$ were pressed into pellets, placed in an alumina tube and sealed in an evacuated quartz ampoule which was heated to 1223 K and held at this temperature for 60 h. The solid-state reactions were repeated with intermediate grinding to improve the sample quality.

Table 3.1: Description of chemical elements used

Chemical element	Formula	Supplier	Purity, %
Iron (pieces)	Fe	Alfa Aesar	99.9
Tellurium	Te	Sigma-Aldrich	99.8
Selenium	Se	Fluka AG	99.999
Thorium dioxide	ThO_2	Ganzhou Mingjie New Material Co., Ltd.	≥ 99.9
Titanium	Ti	Alfa Aesar	≥ 99.9
Titanium dioxide	TiO_2	Alfa Aesar	≥ 99.9
Barium	Ba	Alfa Aesar	≥ 99.9
Arsenic	As	Alfa Aesar	≥ 99.9

3.3 Mössbauer absorbers

In transmission Mössbauer spectroscopy it is necessary to optimize the absorber thickness. First, the maximum signal of nuclear resonance absorption is required with a simultaneous decrease in non-resonant electronic absorption. Both these effects compete with increasing absorber thickness. For an absorber that is too thick the detected radiation has too little intensity and the measurement takes a lot of time or is impossible. For a thin absorber the amount of Mössbauer nuclei can be too small to give a reasonable amplitude of absorption line, which again demands a long time for the experiment. The dimensionless effective absorber thickness is expressed as T [36]

$$T = f_{\mathrm{a}}\eta_{\mathrm{a}}a_{\mathrm{a}}\sigma_0 t_{\mathrm{a}} \tag{3.1}$$

where f_a is the recoil-free fraction of absorption, a_a the fractional abundance of the resonant isotope, n_a the number of Mössbauer nuclei per square centimetre, σ_a the effective cross section for resonance absorption and t_a the thickness of the absorber in cm.

The effective cross-section of nucleus is given as [53]

$$\sigma_0 = 2\pi\lambda^2 \frac{2I_e+1}{2I_g+1}\frac{1}{1+\alpha} \tag{3.2}$$

where α (^{57}Fe: $\alpha = 8.21$) is the internal conversion coefficient of the γ-ray of wavelength λ. I_e and I_g are the nuclear spin quantum numbers of the excited and ground states.

The effective thickness changes with temperature according to the temperature dependence of f_a. The sample must be well ground to make a homogenous powder, the sample powder should be a powder with the consistency close to "talcum powder". We used approximative 50 mg sample powder thoroughly mixed with approximatively 2 drops of a two-component resin (Loctite Power Epoxy) spread evenly on an Al foil pressed in the shape of flat container with a diameter of 20 mm. If there was any bubbles in the mixture, we tried to puncture them. After curing for approximately 10 min the sample was covered with Scotch®Magic^{TM} Tape. This preparation method can be done inside a fume hood.

3.4 Analytical methods

For the study of synthesized sample purity and characterization of the powders the following analytical methods were used: Cu $K\alpha 1$ X-ray powder diffractometry, followed by analysis using the Rietveld method in the FullProf program and ^{57}Fe Mössbauer spectroscopy. Mössbauer spectroscopy enabled us to obtain information on the hyperfine interactions of the synthesized sample. A short description of the methods used are presented below.

3.4.1 X-ray powder diffractometry

The purity and phase composition of polycrystalline samples were checked by X-ray powder diffraction (PANalytical X'Pert Pro MPD diffractometer) at Aalto University in Espoo and at Zhejiang University in China. X-ray diffraction is based on constructive interference of monochromatic X-rays and a crystalline sample. The interaction of the incident rays with the sample produces constructive interference (and a diffracted ray) when conditions satisfy Bragg's Law

$$n\lambda = 2d\sin\theta \tag{3.3}$$

where λ is the coherent wave length, d the distance between the lattice planes and angle θ between the incoming radiation and the lattice plane. The measurements were made in the $\theta - 2\theta$ geometry using Cu $K\alpha 1$ (λ = 1.54051 Å) radiation. Diffraction patterns were registered at room temperature in the beam-angle range of $5 - 110^{\circ}$.

3.4.2 Rietveld method

The Rietveld method [32] is the technique for refining structure and lattice parameters directly from X-ray or neutron diffraction patterns. The Rietveld method can confirm/disprove a hypothetical crystal structure and refine information about a multiphase sample. This is a pattern-fitting method of structure refinement and allows extraction of the maximum amount of information contained in the powder pattern, unit cell parameters for each phase, relative amounts of each phase, atomic positions, fractional site occupancies and preferred orientation. Rietveld refinement allows determinations of positional and thermal parameters from powder data, even when the diffraction peaks are not well separated in the recorded pattern. The crystal-structure refinement was made using the Rietveld method in FullProf program [33] which has been mainly developed for Rietveld analysis for X-ray powder and neutron diffraction data collected with a step width of 0.02 to 0.03° at the scattering angle 2θ. The refinement method uses the profile intensities of the composite peaks instead of the integrated quantities.

The relative intensity of diffraction by Powder method [52]

$$I \cong \frac{1+\cos^2 2\theta}{2} \frac{1}{2\sin^2\theta\cos\theta} F^2 A(\theta). \tag{3.4}$$

where F is the structure factor

$$F_{hkl} = \sum_{j=1}^{m} N_j f_j \exp[2\pi i(hx_j + ky_j + lz_j)] \tag{3.5}$$

where N_j is the fraction of every equivalent position that is occupied by atom j and f_j the scattering factor of the jth atom and $A(\theta)$ the general absorption factor.

The requirements for the use of Rietveld method are:

- high quality experimental diffraction pattern,
- structure model that makes physical and chemical sense and
- suitable peak and background functions (the background is possible to be fixed also manually).

3.4.3 Fit function

Both X-ray and Mössbauer spectra are fitted with a nonlinear least squares fitting routine. The quality of the fit is given by the so-called χ^2 parameter given by [63]

$$\chi^2 = \frac{1}{N-m} \sum_{i=1}^{m} [y(p_j, v_i) - y_i]^2 \frac{1}{y_i} \tag{3.6}$$

where N is the number of data points (256) after folding the Mössbauer spectrum. Each point has specific value y_i at a specific velocity v_i, i = 1,2.....,N and p_j ($j = 1, 2...., m$) is the function of m parameters (δ, B, eQV_{zz})

A successful fitting of parameters p_j causes goodness of fit parameter χ^2 to approach unity.

3.4.4 Mössbauer spectroscopy

The hyperfine interactions in our samples were studied with ^{57}Fe Mössbauer spectroscopy. For Mössbauer measurements we used the equipment of the Mössbauer research group at Åbo Akademi University, with a ^{57}Co:Rh gamma source (Ritverc Co. 25 mCi June 2015, June 2018, and 50 mCi May 2020) in transmission geometry and an LND inc. proportional counter (45431). Calibration was made relative to α-Fe. The low-temperature measurements were made using an Oxford CF506 continuous-flow cryostat with liquid helium between 4.8 –150 K as a coolant and for temperatures 77 –360 K with liquid N_2 as a coolant. The temperature stability was controlled by the Oxford Intelligent Controller ITC 4 and for $T \gtrsim 320$ K using our home-built furnace controlled by a Keithley 2510 TEC SourceMeter. Mössbauer absorber temperature was monitored by home-made Arduino Software (IDE) programmed by Mr. F. Lindroos.

The Mössbauer measurements were carried out in the temperature range of 4.8 –360 K. The obtained spectra were fitted using a home-made non-linear least squares fitting software employing

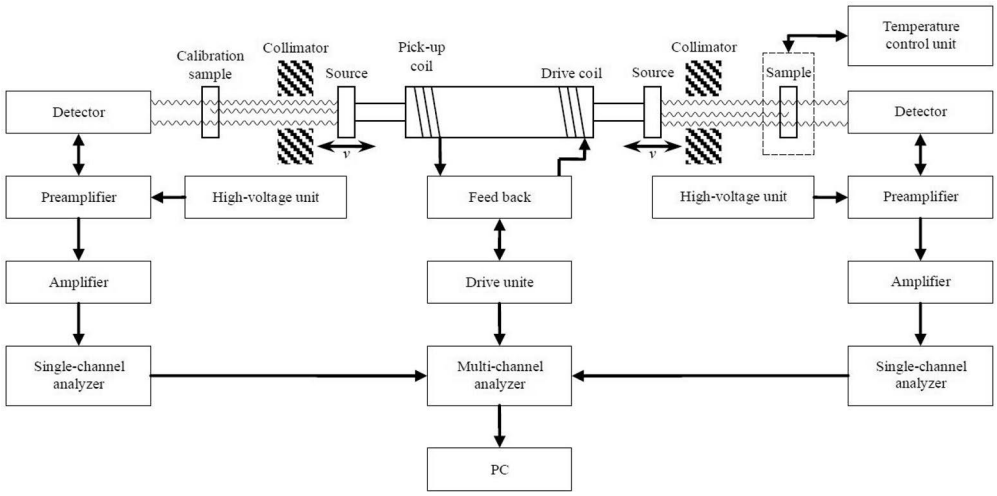

Figure 3.1: Schematic view of a Mössbauer spectrometer setup.

the full Hamiltonian of electric and magnetic hyperfine interaction and some spectra were also controlled with transmission integral analysis with the MossWinn 4.0 program [34]. A small amount of Fe impurity in the beryllium window, seen as a weak symmetric doublet, is not included in the calculations.

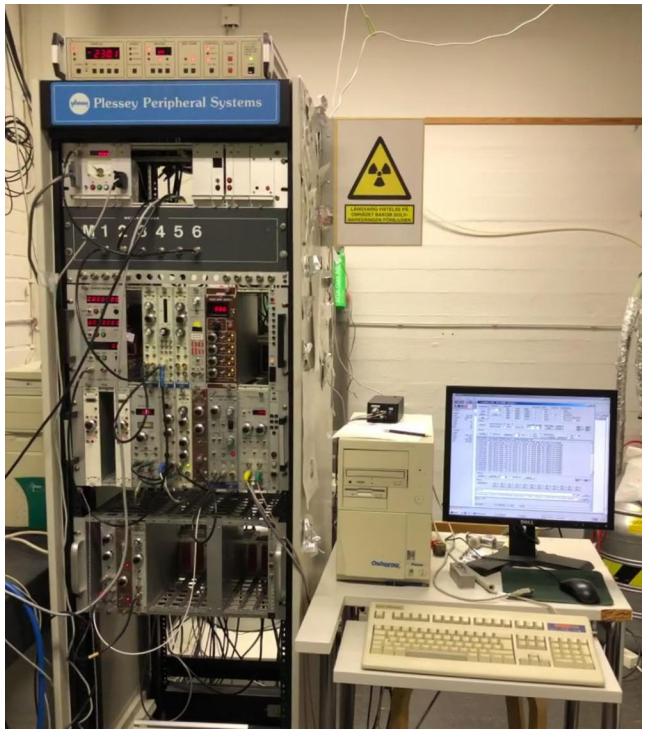

Figure 3.2: Mössbauer spectrometer component rack.

Figure 3.3: Cryostat and dewar for liquid N_2.

CHAPTER IV

Mössbauer study of magnetism in Fe_3Se_4

4.1 Motivation

We have a "mysterious" FeSe phase whose structure and properties are also unknown. This got us to study more closely the FeSe phase. We also were interested to check if the Fe_3Se_4 phase could be related to an elusive FeSe [6] phase observed by some of the members of the group, we decided to make a Mössbauer study of the magnetism in Fe_3Se_4. The phase diagram of ironselenides is rather complicated [1]. Among the known Fe-Se phases there are also phases, which are magnetically ordered around room temperature e.g. Fe_7Se_8 [4] and Fe_3Se_4 [5]. For Monoclinic Fe_3Se_4 with a NiAs-type crystal structure H. Okamoto [1] reported a rather narrow solid-solution compositional range of 55.4-56.8 at.% Selenium. Fe_3Se_4 has several interesting properties. It has e.g. been suggested that Fe exhibits valence mixing similar to magnetite (Fe_3O_4) with an analogous charge balance of $Fe^{3+}Fe_2^{2.5+}Se_4^{2-}$, i.e. Fe at site 2 exhibits valence mixing [5, 7]. The ratio between the populations at the two Fe sites is 1:2. Slightly above room temperature Fe_3Se_4 undergoes a transition into an antiferromagnetically coupled structure, observed e.g. by neutron diffraction [9, 10]. However, as the spins do not cancel the overall phase is ferrimagnetic, with a Curie temperature (T_C) of 327 to 357 K, depending on the composition. The monoclinic structure does not change when the phase undergoes the magnetic transition [5]. The magnetic moments of the Fe atoms are comparatively low, judging by neutron diffraction [5, 11] data: $3.25\mu_B$ for site 1 and $1.94\mu_B$ for site 2. Although Fe_3Se_4 has been studied since the 1950s its hard magnetic property remained unattended for a long time [14]. Hard magnets have a high coercivity H_c, and thus retain their magnetization in the absence of an applied field. This gives a wide range of applications for example in data processing [54].

4.2 Characterization of Fe_3Se_4

4.2.1 X-ray diffraction

Powder X-ray diffraction data used for phase identification were collected at room temperature on a PanAnalytical X'Pert Pro MPD diffractometer using Cu $K\alpha 1$ radiation. Rietveld analysis based on the monoclinic $I2/m$ (#12) space group for Fe_3Se_4 was used to confirm the origin of the observed peaks in the diffraction pattern. The X-ray diffraction pattern and the unit cell of the

$FeSe_{1.2779}$ sample are displayed in Fig. 4.1. All observed peaks can be indexed with reflections of the monoclinic Fe_3Se_4 structure [5, 12]. Possible impurities are therefore well below the detection limit. The fitted values for the lattice parameters were $a = 6.20238(3)$ Å, $b = 3.53183(2)$ Å, $c = 11.33099(6)$ Å, and $\beta = 91.8252(3)^\circ$. Rietveld analysis gave a 1:2 ratio for the iron lattice sites 1 and 2.

4.2.2 Mössbauer spectra

The magnetic properties of the $FeSe_{1.2779}$ sample were characterized using ^{57}Fe Mössbauer spectroscopy in transmission geometry. 48 mg of the ground sample $FeSe_{1.2779}$ was used for the absorber. The spectra were measured between October 2015 and February 2016 using ^{57}Co:Rh source (Ritverc Co. 25 mCi Sept. 2015) with a maximum Doppler velocity of 1.75-6.5 mm/s at temperatures between 77 and 360 K. Each spectra was measured for 48 h, where the lower velocities were used for following the demise of the magnetic hyperfine field. The sample was cooled using an Oxford CF506 continuous-flow cryostat with liquid N_2 as coolant. Temperatures above 330 K were reached using a home-built resistive heater, flushed with a small stream of dry N_2 gas to prevent sample oxidization. The heater was controlled using a Keithley 2510 TEC SourceMeter.

Initially, all magnetic spectra were fitted using four Mössbauer components, although the Rietveld data suggests that two should be enough. Each component would represent a specific Fe species in the lattice. Below T_C each component consists of a six-line spectrum analyzed using the following fit parameters: magnetic hyperfine field B acting on the Fe nucleus, electric quadrupole coupling constant eQV_{zz}, asymmetry parameter η, the angle β between the direction of B and V_{zz}, the isomer shift δ relative to α-Fe, and relative component intensity I. The line width Γ was fitted but constrained equal for all lines and components.

When fitting the spectra neither the high- nor the low-field part could be completely explained by four component each. We also tried to analyse the internal hyperfine field by helical magnetism [22]. The idea was to make the internal field dependent on a rotation angle θ,

$$B = B_0 f(\theta) \tag{4.1}$$

but the statistical χ^2 parameter (The Goodness of the fits parameter) for the fitted spectra remained very high. Minimizing χ^2 is the main task of all fit programs. A succesful fitting of parameters causes χ^2 to approach unity.

In a second attempt the number of Mössbauer components were reduced to two. To cope with the spectrum shape, histogram distributions, effectively modulating the local iron valence were introduced for each component. A parameter interval $q \in [0, 1]$ was divided into partitions q_i, with i running from 1 to 20. One may think of q as a charge associated with the Fe ion. As the unit of the q is arbitrary, the absolute width of the interval in charge units is not fixed. Each q_i was given a none-negative weight h_i taken as a fit parameter. The isomer shift and quadrupole coupling have a direct dependence on the iron charge, while the internal field depends indirectly upon it through the electron spin. Hence, when fitting eQV_{zz}, δ, and B the following generic expression was used for each temperature-dependent hyperfine parameter:

$$p_i(T) = p_0(T) + \alpha(T)q_i \tag{4.2}$$

where $p_0(T)$ is the value of the hyperfine parameter if the histogram is omitted, *i.e.* it gives the value for the hyperfine parameter in the absence of the valence modulation and $\alpha(T)$ scales the span

of distribution. In this manner the distribution for all hyperfine parameters for a specific iron site depend on the same charge histogram. Two such histograms where used - one for each lattice site. Effectively each Mössbauer component consists of twenty sub-components with a statistical weight given by the relative height h_i of each partition q_i, with the additional requirement that $\sum_i h_i = 1$. The Mössbauer spectrum recorded at 110 K is displayed in Fig. 4.2.

In the upper panel of Fig. 4.2 the fitting was done using four sextets and in the lower using only two, but with distributions for the hyperfine parameters. Using only two simple sextets with no distributions yielded poor fittings and was therefore immediately abandoned. In the four-component fitting one of the two low-field components exhibited excessive broadening, which is curious as it should originate from the same iron site as the other low-field component, which did not exhibit broadening. This effect disappeared when the number of components was reduced to two and hyperfine parameter histograms were released. Furthermore, the experimental line width Γ remained close to the "thin-absorber limit" around 0.25 mm/s, or slightly below, except around T_C where the spectra were slightly broadened and Γ reached 0.30 mm/s. In the paramagnetic regime Γ returned to $\sim$ 0.25 mm/s. Throughout the temperature range the intensity ratio for the two components remained close to 2:1, Fig. 4.3. Only around T_C some deviations occurred.

Independent of the fitting scheme the values of the average field $\langle$ B $\rangle$ are too low for regular high-spin Fe^{3+} or Fe^{2+} with $B \approx 23$ T for site 1 and $B \approx 8$ T for site 2, Fig. 4.4. Typical spin-only saturation values are ~ 53 T for Fe^{3+} and ~ 42 T for Fe^{2+}, as trivalent iron has five majority-spin electrons and the divalent additionally one minority-spin electron. Such fields correspond to iron magnetic moments of $\sim 5\mu_B$ and $\sim 4\mu_B$, respectively. The average valence of Fe, assuming Se^{2-} is +2.67, which would bring the internal field slightly down from the high-spin trivalent value. The coordination octahedron around site 1 is rather regular and hence the crystal-field splitting ought to be moderate, while the coordination octahedron around site 2 is much more deformed and this could give rise to substantial crystal-field splitting, which could cause Fe to reside in an intermediate-spin state. As the magnetic fields are low most probably both Fe species are in the intermediate spin-state, in which case also dipolar and orbital contributions could be present, further counteracting the regular spin contribution.

A dipolar contribution arises if the co-occupancy of the minority and majority-spin electron is confined to a particular d-orbital, instead of being symmetrically distributed on several orbitals. This would then bring down the internal field considerably as a dipolar contribution can be several tens of Tesla.[17]
As Fe_3Se_4 is probably more covalent than ionic it is hard to make reliable estimates of the contributions to the internal field, even the spin-only contribution mediated by the Fermi-contact interaction may vary. As high-spin Fe^{3+} has a magnetic moment of 5 μ_B the intermediate-spin magnetic moment is 3 μ_B, but when the formal valence is +2.67 the intermediate magnetic moment and corresponding internal field could be roughly 3.33 μ_B & 35,3 T or 2.67 μ_B & 28.3 T, depending on how the fractional valence affects the moment. Interestingly the ratio of these two extremes is not too far off from that obtained from neutron scattering: 3.25:1.94 [9] for the two Fe sites. Dipolar contributions cannot be observed by neutron scattering, but if we surmise that the above two estimates for the magnetic moments correspond to the two Fe sites, then an antiparallel dipolar field of ~ 13 T or ~ 20 T is acting on Fe nuclei, depending on if the neutron-scattering values or the estimated values are used. These are not inconceivably large for a dipolar field caused by a non-spherical, i.e. an intermediate-spin configuration.

The 77-K isomer shift values (Fig. 4.5) of 0.78 mm/s for site 1 and 0.70 mm/s for site 2 are both

slightly shifted towards divalency, in particular the former. Both values are compatible with the intermediate spin state, shifted slightly towards divalency due to the fractional valence state [36].

While the magnetic fields are rather low, the experimental quadrupole coupling constants (Fig. 4.6) are rather substantial, i.e. the d-electron influence on both the electric and magnetic hyperfine interactions were large. Therefore, the angle β and the asymmetry parameter η could be released in the fittings. Generally β was very close to $-90°$ for Fe at site 1 and $+90°$ for site 2. Point-charge calculations for the selenium ions contribution to the electric field gradient acting on the Fe nuclei gave rather modest values for V_{zz}, indicating that there must be a substantial valence electron contribution, no doubt caused by the intermediate-spin configuration, because a substantial dipolar contribution is also connected to a large valence-electron contribution to the electric field gradient.[17]

Non-zero η values are to be expected for a monoclinic structure, but generally η is notoriously hard to fit reliably. Except around T_C η remained close to 0.6 for site 1 and 0.4 for site 2, *i.e.* it was surprisingly stable. The histograms for the magnetic fields obtained from the fittings are displayed in Figs. 4.7 and 4.8.

Histograms for the quadrupole coupling constant Figs. 4.9 and 4.10 and for the isomer shift Figs. 4.11 and 4.12 are almost identical to the magnetic one, except that the span and midpoint of the x-axis is different, in accord with eq. 4.2. They also reach to temperatures beyond T_C, whereas for the magnetic field $p_0(T_C) = \alpha(T_C) = 0$, as the internal fields are zero above T_C. The Curie temperature interpolated from the field data is 331 K, Fig. 4.4. For both sites the histogram of the magnetic field is peaked around two separate field values, explaining why the four-component fitting was also successful. Such double peaks can be taken as a sign that there is a two-peaked distribution of the valence within the iron site.

Average hyperfine parameters for each iron site are readily obtained by summing up the contributions in Eq. 4.2:

$$\langle p_i(T) \rangle = p_0(T) + \alpha(T) \sum_{i=1}^{20} h_i q_i. \tag{4.3}$$

The hyperfine parameters plotted as a function of temperature, in Figs. 4.3, 4.4 , 4.5 and 4.6 were obtained by applying Eq. 4.3 to the histogram data. Interestingly, the histograms are needed also above T_C, as it is impossible to fit the data using only two paramagnetic doublets of to the two sites. In this region our four-component fitting failed, as it was not possible to find a combination retaining the 1:2 intensity ratio by grouping the components in two pairs. However, the histogram distributions become narrower at T_C and practically point-like for site 2, while site 1 still exhibits a substantial spread. A paramagnetic spectrum recorded at 360 K, is displayed in Fig. 4.13 and the spreading of component 1 is evident.
In the region just below T_C the fitting becomes increasingly difficult, as the fluctuating atomic spins cause the internal field distributions to blur. Thus the sudden drop for the quadrupole coupling constant of Fe at site 1 may be a simple artifact of fitting, Fig. 4.6, but the cross over seems to be a real effect. The isomer shifts, Fig. 4.5 exhibit a more monotonic decrease, typically caused by the temperature-dependent second-order Doppler shift.[18] Above T_C the isomer shifts of the two components converge, which may indicate that the paramagnetic moments of site 1 and 2 converge. Above T_C the isomer shift values have crossed like the quadrupole coupling constants, which could indicate a slight charge transfer between the iron sites, enabled due to the disappearance of the antiferromagnetic coupling between the two Fe sites.

Fe_3Se_4 was further investigated in publication VI (Girish C. Tewari et al. Fe_3Se_4 A Possible Ferrimagnetic Half-Metal?, Journal of Physics: Condensed Matter, **32** (2020) 455801) because mixed valence and ferrimagnetism are interesting and potentially applicable.

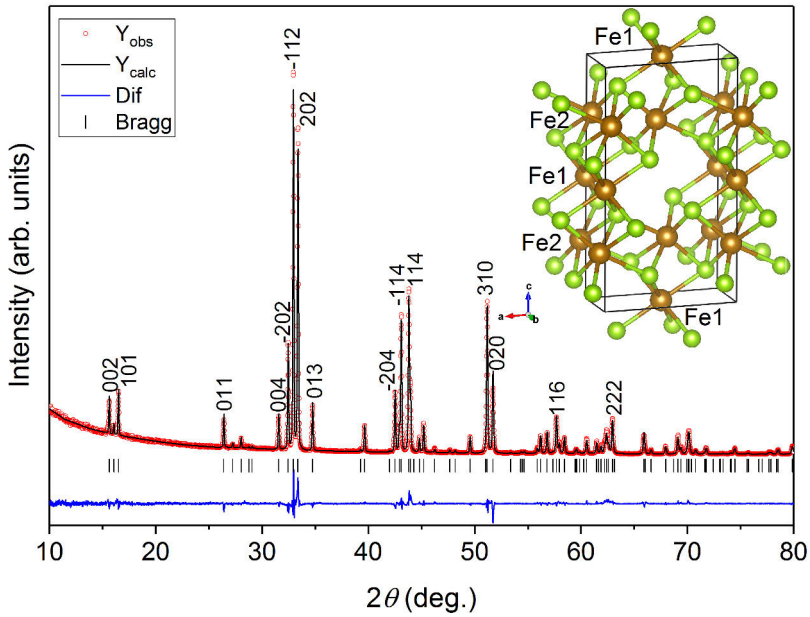

Figure 4.1: Fitted X-ray diffraction pattern for $FeSe_{1.2779}$. Ticks denote the positions of the identified peaks and the difference between fitting and data is displayed below the ticks. Main reflections are indexed up to $2\theta \approx 65°$. Inset: The unit cell of Fe_3Se_4, with Fe atoms in brown and Se atoms in green.

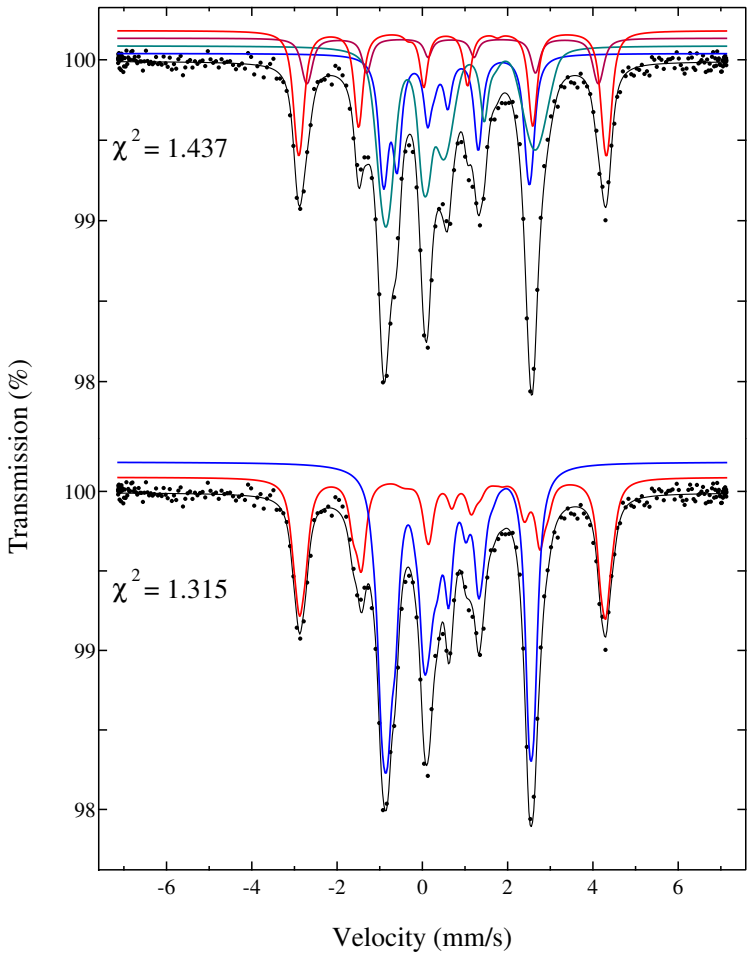

Figure 4.2: Mössbauer spectrum of the $FeSe_{1.2779}$ sample recorded at 110 K fitted using four components (upper panel) and two components with histogram distributions for the hyperfine parameters (lower panel), see text. The reddish (large internal field) components are assigned to Fe at site 1 and the bluish (low internal field) to Fe at site 2.

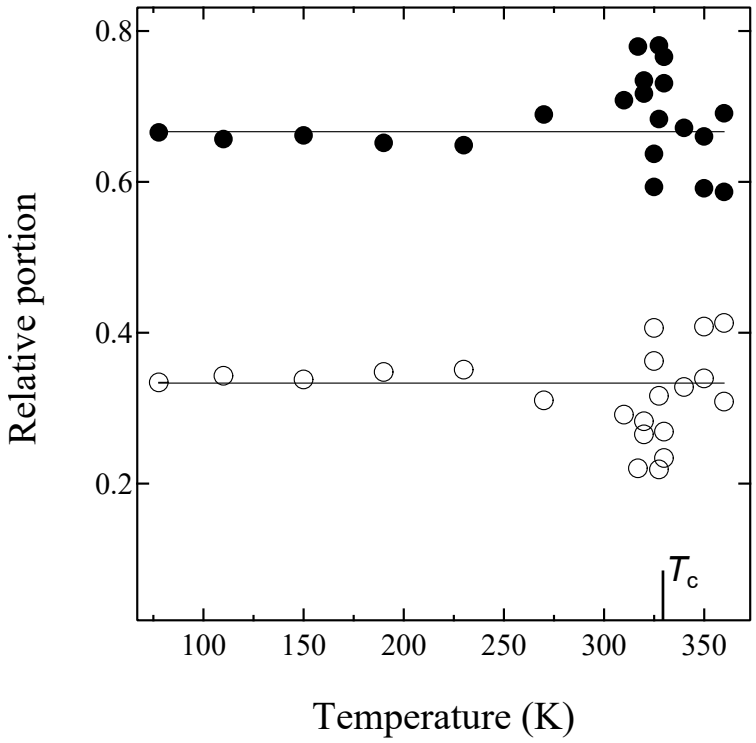

Figure 4.3: Relative intensities for the two components, originating from site 1 ○ and site 2 ●. Horizontal lines indicate the theoretical intensities corresponding to the multiplicity of the two sites.

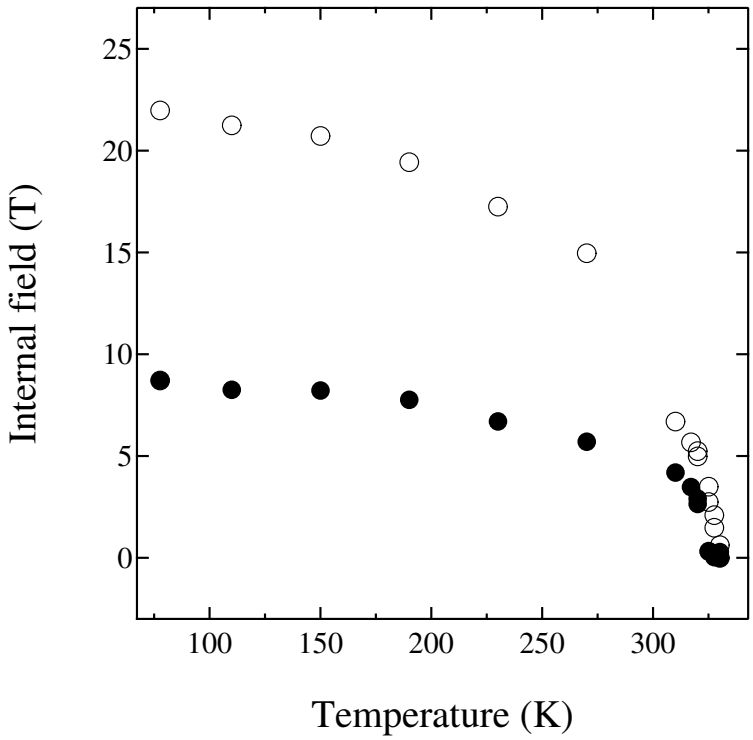

Figure 4.4: Average internal field for Fe at site 1 ○ and site 2 ●.

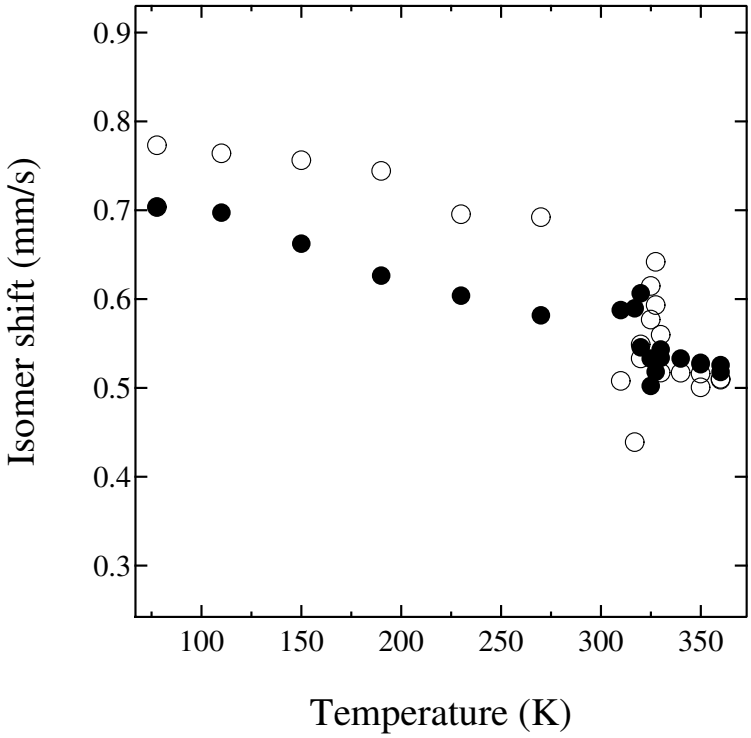

Figure 4.5: Average isomer shifts for Fe at site 1 ○ and site 2 ●.

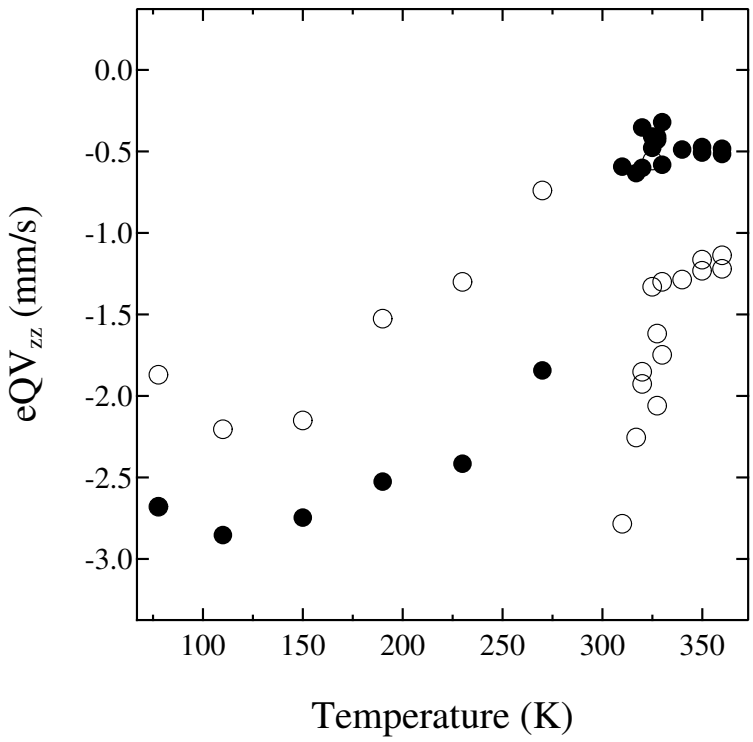

Figure 4.6: Average quadrupole coupling constants for Fe at site 1 ○ and site 2 ●.

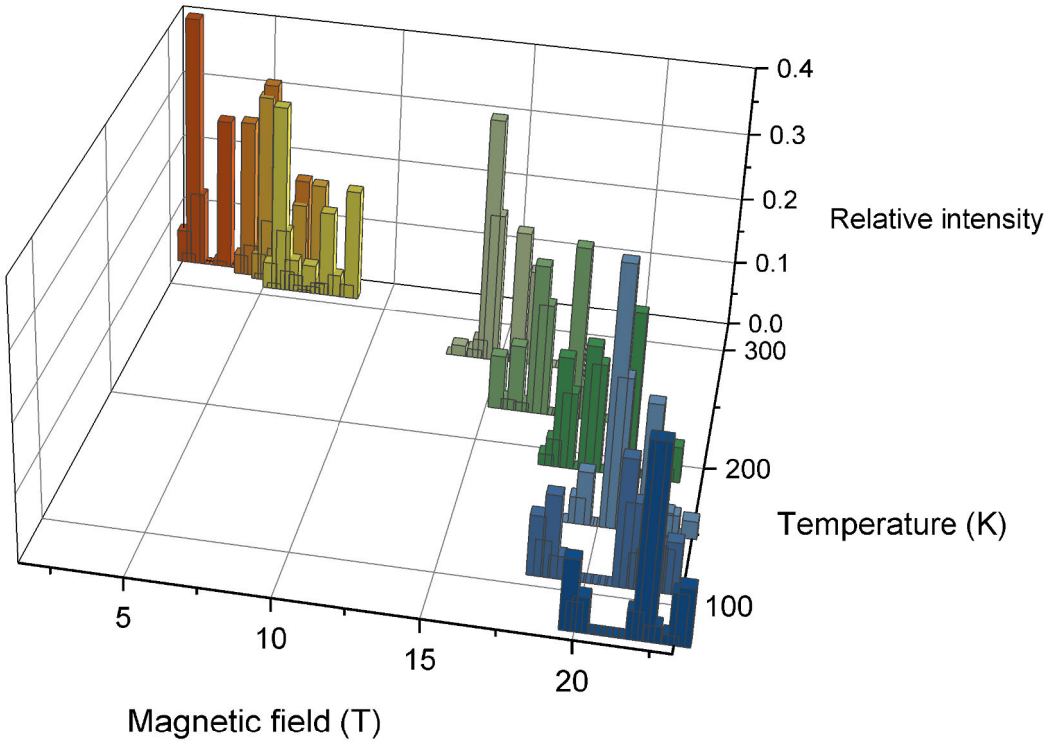

Figure 4.7: Histogram for internal magnetic field of Fe at site 2 vs. temperature. The histogram data was obtained by fitting the Mössbauer spectra, see text for details.

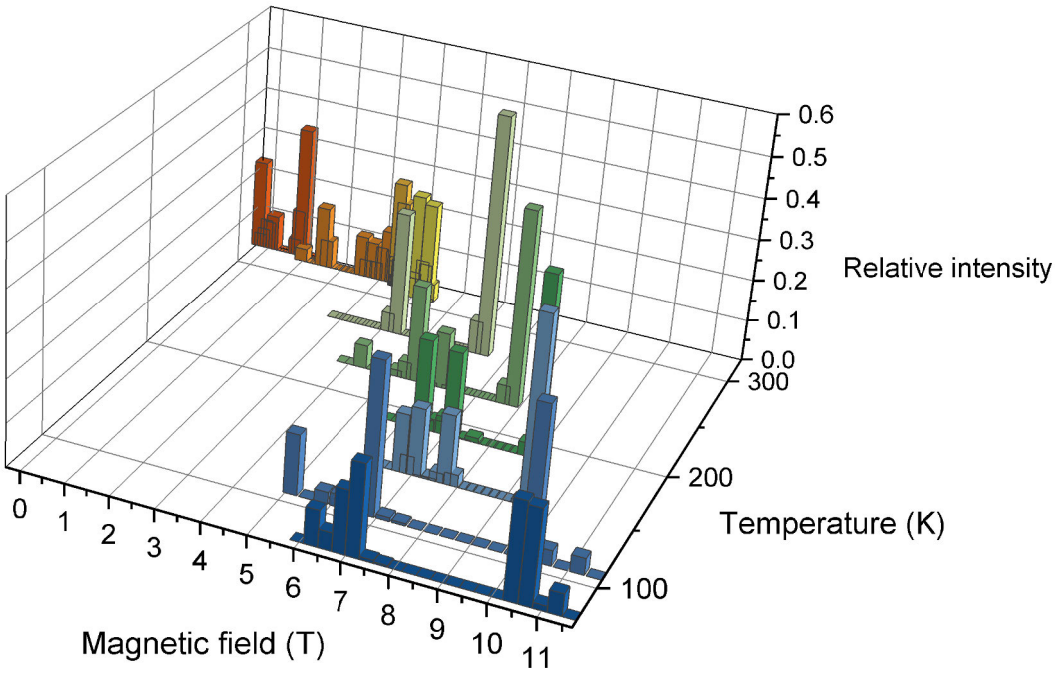

Figure 4.8: Histogram for internal magnetic field of Fe at site 1 vs. temperature. The histogram data was obtained by fitting the Mössbauer spectra, see text for details.

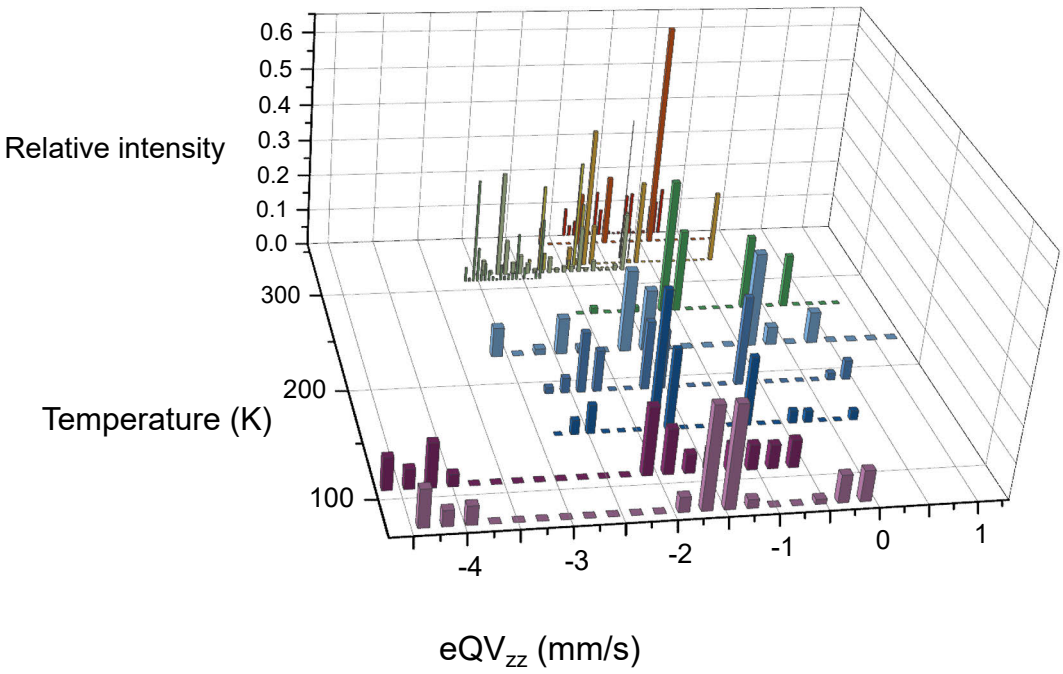

Figure 4.9: Histogram for quadrupole coupling of Fe at site 2 vs. temperature. The histogram data was obtained by fitting the Mössbauer spectra, see text for details.

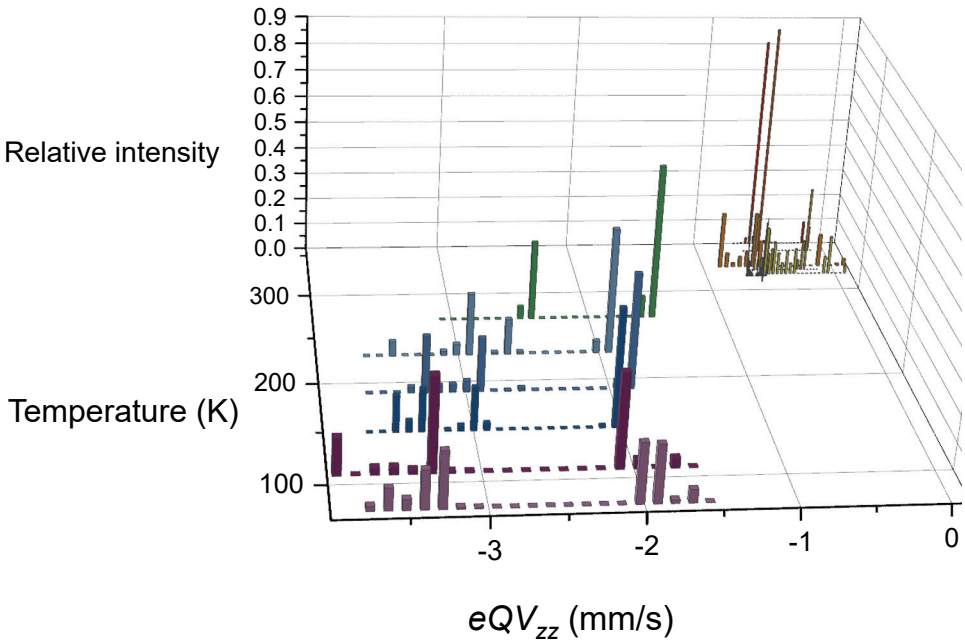

Figure 4.10: Histogram for quadrupole coupling of Fe at site 1 vs. temperature. The histogram data was obtained by fitting the Mössbauer spectra, see text details.

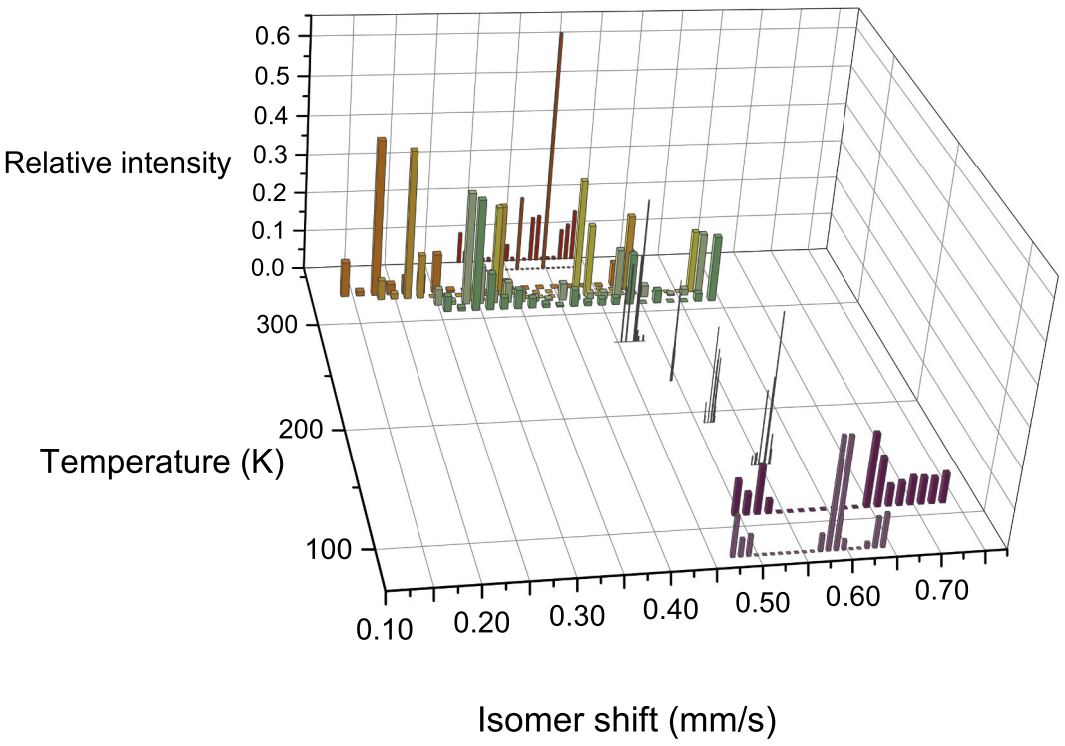

Figure 4.11: Histogram for isomer shift of Fe at site 2 vs. temperature. The histogram data was obtained by fitting the Mössbauer spectra, see text for details.

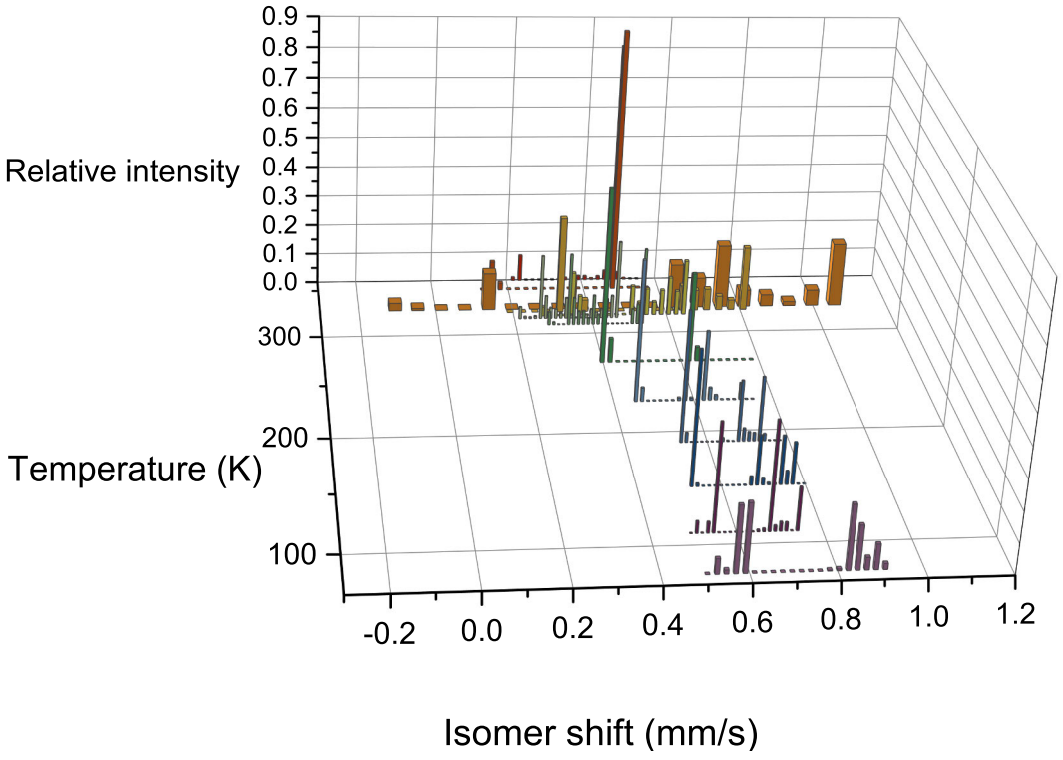

Figure 4.12: Histogram for isomer shift of Fe at site 1 vs. temperature. The histogram data was obtained by fitting the Mössbauer spectra, see text for details.

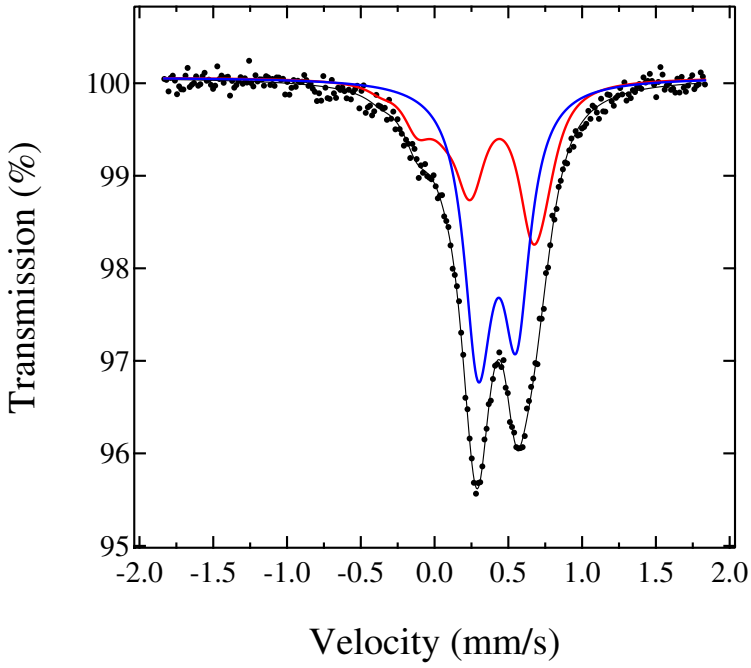

Figure 4.13: Mössbauer spectrum of the $FeSe_{1.2779}$ sample recorded at 360 K fitted using two components with histogram distributions for the hyperfine parameters, see text. The red (low intensity) component is assigned to Fe at site 1 and the blue (high intensity) to Fe at site 2.

CHAPTER V

Investigating the vibrational lattice anisotropy in $FeTe_{0.5}Se_{0.5}$

5.1 Motivation

Usually the material provided by nature (minerals, biological samples, physical metallurgy, etc.) [30] are already partially texturized. Due to texturizing the quadrupole-split doublet of the Mössbauer spectra have a characteristic asymmetry, which can be removed by turning the sample into the so called magic angle ($\approx 54.7°$) with respect to the direction of the incoming Mössbauer γ-ray beam. Sometimes powdered crystallites can be oriented using an external magnetic field and fixed in the desired direction by letting a mixture of powder and a bonding agent harden in the field. In order for this to work the magnetic susceptibility must exhibit an anisotropy along the crystalline directions. The method has been used *e.g.* for high-T_c cuprate superconductors [28]. The aim of our work was to study lattice anisotropy of $FeTe_{0.5}Se_{0.5}$ using magnetically oriented crystallites, with c axes parallel and normal to the sample surface.

5.2 $FeTe_{0.5}Se_{0.5}$ absorbers

The as-prepared powder was re-ground and three Mössbauer absorbers were made.

For Sample 1; ~ 55 mg of powder was mixed with a 15-min epoxy glue, spread evenly on a flat cylindrical Teflon mold and immediately placed for an hour in a horizontal position to harden in the vertical 11.7 T field of a strong magnet. For this purpose a Bruker Ultra-High-Field NMR magnet was used.
For Sample 2; ~ 55 mg of powder was mixed with epoxy glue, spread evenly on a Teflon mold and quickly placed in the Bruker Ultra-High-Field NMR magnet field of the magnet. A self-constructed gearbox mechanism, made of plastics and Lego® parts allowed the sample to be rotated around a horizontal axis perpendicular to the field (Fig. 5.1). The sample was rotated for 1 hour until the sample-glue mixture had hardened completely.
For Sample 3; ~ 28 mg of the powder mixed with epoxy glue was spread evenly on an Al foil and left to harden under ambient conditions.

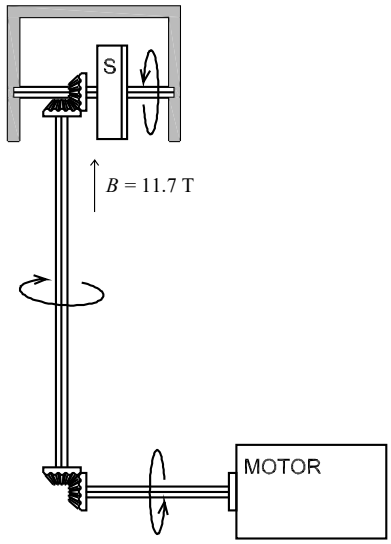

Figure 5.1: Sketch of the mechanism for rotating the powder and epoxy mixture inside the Teflon cup marked by S. Cogwheels and axles were made of Lego® parts.

5.3 Characterization of $FeTe_{0.5}Se_{0.5}$

5.3.1 X-ray diffraction

The phase and structure determination of the as-synthesized powder and the magnetically aligned absorbers were carried out at room temperature with a X-ray powder diffractometer (PanAnalytical X'Pert Pro MPD) using Cu $K\alpha 1$ radiation. Data were analyzed by the Rietveld method using the FullProf program [33]. The room-temperature X-ray diffraction patterns for the samples are shown in Fig. 5.2 along with theoretical curves obtained by Rietveld analysis and the difference curves between data and fitting. The analysis reveals the presence of the main phase $FeTe_{0.5}Se_{0.5}$ and, as a minority phase, no more than $\sim 3\%$ of orthorhombic FeSe, not enough to be detectable in the Mössbauer spectra. No lower-symmetry phases were observed, *i.e.* quenching did not promote the appearance of additional phases, as it does for $Fe_{1-x}Se_x$ [31]. The observed FeSe impurity had a slightly shorter c axis than reported in literature for orthorhombic FeSe [35]; $\sim 5.657(1)$ Å instead of 5.805 Å. It also exhibits a remarkable inclination for texturizing. In Sample 1 FeSe exhibited an almost complete $00l$ texturizing according to the Rietveld analysis, and is therefore very visible in Fig. 5.2, middle panel.
Interestingly, regular tetragonal FeSe orients perpendicular to an external field. $FeTe_{0.5}Se_{0.5}$ has a crystal symmetry described by a tetragonal PbO structure with $P4/nmm$ space group (129). The fitted values for the lattice parameters were $a = 3.8007(1)$ Å and $c = 5.9741(2)$ Å. Iron occupies site $2a$: (3/4,1/4,0) and Te/Se site $2c$: (1/4,1/4,z), with z fitted to 0.2747(2) in Sample 2 and 0.2664(5) in Sample 3.
The statistical parameter χ^2 ranged from 5.05 for Sample 2 to 11.5 for the as-synthesized powder.

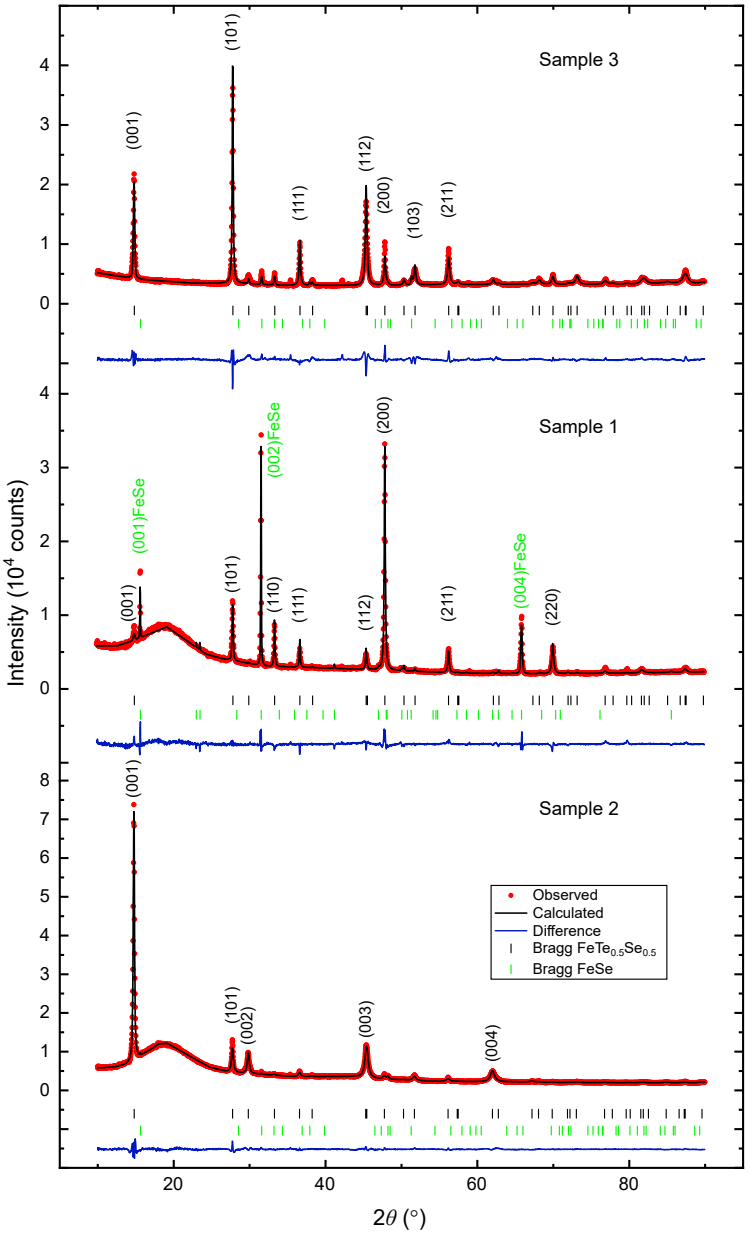

Figure 5.2: Room-temperature XRD patterns indexed with Miller indices for the tetragonal PbO structure of the $FeTe_{0.5}Se_{0.5}$ iron chalcogenide phase and for the minority phase FeSe. An amorphous background caused by the epoxy glue is visible for Samples 1 and 2.

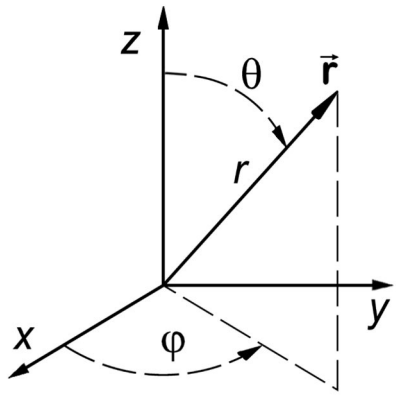

Figure 5.3: Spherical coordinate system with $x = r\sin\theta\cos\phi$, $y = r\sin\theta\sin\phi$, $z = r\cos\theta$, angle θ is the angle between the z axis and the wave vector $\vec{k}$ of the emitted γ-ray.

Sample 1, was placed for an hour in a horizontal position to harden in the vertical 11.7 T field of an NMR magnet. Thus the field was parallel with the sample normal and prominent $(hk0)$ reflections are observed for the main phase in Fig. 5.2. The angle θ between the sample normal and the c axes is peaked around 90°, suggesting that the c axes are oriented parallel ($\parallel$) to the sample surface.
In Paper II, the θ angles of Sample 1 and Sample 2 are crossed with each other, but the analysis is nevertheless correct. In Sample 2, continuously rotated vertically in the sample cavity of the magnet Fig. 5.1, the $(00l)$ reflections are well observed suggesting that the c axes are oriented perpendicular ($\perp$) to the absorber surface and the angle θ between the sample normal and the c axes is peaked around 0°.
In contrast to this, the minority phase FeSe orients parallel to an external field and in Sample 1 exhibit $(00l)$ reflections. It should in Sample 2 have $(hk0)$ peaks if there were reflections strong enough.

By fitting the textures of $FeTe_{0.5}Se_{0.5}$ in Sample 1 and 2 it was possible to determine the spatial distribution of the c axes. The following experimental distribution function was used for the magnetically oriented samples (Eq. 3.31 in the Introduction to the program FullProf 2000 Version July 2001, Juan Rodriguetz-Carvajal)

$$D(\theta) = a + (1-a)e^{b\theta^2}, \tag{5.1}$$

where θ is the angle between the c axis and the normal of the sample surface, a represents the randomly oriented fraction and b defines the width of the distribution of the oriented fraction. For Sample 1 ($hk0$ reflections dominate) b is positive, *i.e.* the function peaks at $\theta = 90°$, while for Sample 2 ($00l$ reflections dominate) b is negative, *i.e.* the function peaks at $\theta = 0°$. Parameter values for $a,\ b$, were directly obtained from the FullProf program: $a = 0.88(2)$, $b = 2.35(3)$, and $a = 0.0336(4)$, $b = -12.5(2)$, for Samples 1 and 2, respectively. An additional normalization of

$$N^{-1}\int_0^{\frac{\pi}{2}} D(\theta)\sin\theta d\theta = 1 \tag{5.2}$$

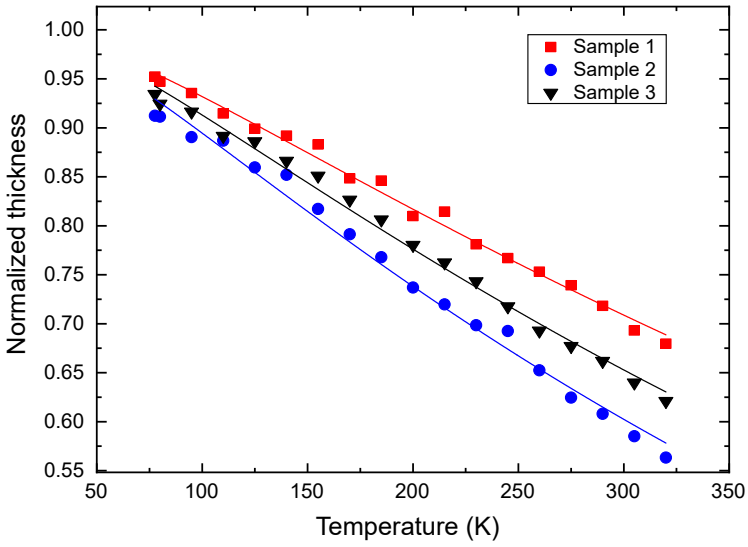

Figure 5.4: Mössbauer thicknesses vs. temperatures fitted using the Debye model for the f_a factor. The data was normalized to unity at 0 K. Sample 1, preferentially oriented with $\mathbf{k}_\gamma \perp c$, has the highest Debye temperature and Sample 2 oriented with the preference $\mathbf{k}_\gamma \parallel c$ has the lowest. Sample 3, which was allowed to sediment and was turned 40° in the beam, lies between these. Statistical errors do not exceed the size of the symbols.

was imposed for the distribution $D(\theta)$. The normalization parameter was $N = 6.7(8)$ and $0.0717(9)$ for Sample 1 and 2, respectively. The untexturized background covered 13(2)% (47(1)%) of the grains in Sample 1 and 2.

Also the atomic displacement parameters of the main phase were fitted in the Rietveld analyses. As the chalcogenide site is co-occupied by the Se and Te elements, the displacement parameter is not very reliable for them. For the iron site displacement parameters of $B = 0.70(9)$ Å^2 and $B = 1.80(9)$ Å^2 were obtained for Sample 1 and 2, respectively. For Sample 3 we applied an anisotropic displacement parameter for iron, yielding $B_{11} = B_{22} = 1.3(4)$ Å^2 and $B_{33} = 2.8(4)$ Å^2. These values indicate the presence of a lattice anisotropy with the largest displacement along the c axis.

5.3.2 Mössbauer spectra

Mössbauer spectra were recorded with maximum Doppler velocities of ~ 2.0 mm/s calibrated with α-Fe. Spectra were measured in transmission geometry in the temperature interval $77-320$ K using an Oxford CF506 continuous-flow cryostat with liquid N_2 as coolant and a ^{57}Co:Rh source (Ritverc Co. 25mCi June 2018). The spectra were fitted using the MossWinn 4.0 program [34] with the following Mössbauer parameters released in the fitting: the quadrupole coupling constant eQV_{zz}, the relative component intensities, the isomer shift δ relative to α-Fe, and the average angle θ_{ave} between V_{zz} and the direction $\mathbf{k}_\gamma$ of the γ-ray beam. The spectra were fitted using transmission integrals and

hence also the so-called Mössbauer thickness of the samples was fitted in order to determine the recoil-free absorption factor f_a. For the Mössbauer measurement Sample 3 was positioned at an angle of $\sim 40^\circ$ with respect to $\mathbf{k}_\gamma$, in order to decrease sedimentation-induced texture effects. The increase in the effective thickness had been anticipated in advance by using a smaller amount of powder for this sample. At room temperature $eQV_{zz} = -0.58(1)$ mm/s and directed along the c axis, while $\delta = 0.460(1)$ mm/s, in accord with literature [27]. The sign of V_{zz} is readily confirmed using Samples 1 and 2 and the XRD-data. In order to prove presence of GKE in the present samples we measured a temperature series for all three samples. The 77.6 K Mössbauer spectra are shown in Fig. 5.5.

The average angle between V_{zz} and $\mathbf{k}_\gamma$ was fitted to $\theta_{\text{ave}} = 62(1)^\circ$ for Sample 1, $42(1)^\circ$ for Sample 2, and $52.6(5)^\circ$ for Sample 3. All spectra where fitted using transmission integrals and the thus obtained Mössbauer thicknesses are presented in Fig. 5.4. The data is normalized to unity at 0 K, as the sample thicknesses [36] were not identical, but similar to within $\pm 10\%$.

The calculated sample thickness, Eq. 3.1, did not exceed 2 for any of the samples, *i.e* they can be regarded as thin [36].
The data of Fig. 5.4 was fitted using the Debye model for the recoil-free fraction Eq. 2.15.

Owing to the exponential dependence neither the normalization nor the values of the constants in Eq. 2.15 affect the fitted values of the Debye temperature. The highest value for the Debye temperature $\theta_D = 303(3)$ K was obtained for Sample 1 and lowest $\theta_D = 255(3)$ K for Sample 2, while for Sample 3 at $\sim 40^\circ$ $\theta_D = 275(3)$ K was between Sample 1 and Sample 2.
At 0 K, the corresponding recoil-free fractions are: $f_a = 0.894(1)$, 0.875(2) and 0.884(1) for Samples 1, 2 and 3, respectively. This indicates that the recoil-free fraction f_a is largest in the ab plane and smallest along the c axes, i.e that $FeTe_{0.5}Se_{0.5}$ indeed exhibits GKE.
Using the Debye temperatures we can now estimate the recoilfree fractions along the c axis and in the ab plane at 0 K, using the expression for an axially symmetric recoil-free fraction $f_a(\theta)$, which is given by [30]:

$$f_a(\theta) = \exp[-k_\gamma \langle x_\perp^2 \rangle - (k_\gamma \langle x_\parallel^2 \rangle - k_\gamma \langle x_\perp^2 \rangle) \cos^2 \theta], \tag{5.3}$$

where $\langle x_\parallel^2 \rangle, \langle x_\perp^2 \rangle$ are the mean square displacements along c axes and in the ab plane, respectively and k_γ the magnitude of the γ wave vector. By inserting the θ_{ave} angles from the Mössbauer fittings and recoil-free fractions for Samples 1 and 2 into Eq. 5.3 we can solve and obtain $\exp(-k_\gamma \langle x_\perp^2 \rangle) = 0.907(2)$ and $\exp(-k_\gamma \langle x_\parallel^2 \rangle) = 0.851(6)$, for the f_a factors in the ab plane and along the c axis, respectively. Keeping these values fixed and inserting $\theta = \theta_{\text{ave}} = 52.6^\circ$ for Sample 3 into Eq. 5.3 we get $f_a = 0.886(4)$, which agrees with the experimental value for Sample 3 given above.

Having observed the GKE, it is interesting to check whether the second-order Doppler shift of the isomer shift data also exhibits this anisotropy. In Fig. 5.6 the isomer shift data fitted with the Debye model for the second-order shift is plotted. The temperature-independent true isomer shift δ_0 was constrained equal in the fit function Eq. 2.7 for the isomer shift.

Upon fitting the data $\delta_0 = 0.6903(7)$ mm/s was obtained, and a small anisotropy for the Debye temperature also: $\theta_D = 428(5)$ K for Sample 1 and $\theta_D = 410(5)$ K for Sample 2. Again, for Sample 3 at $\sim 40^\circ$ $\theta_D = 414(5)$ K was between these.

The discrepancy in the Debye temperatures obtained from the isomer-shift data and the absorption data is not unusual and indicates that the Debye model is only an approximation. As the exponents

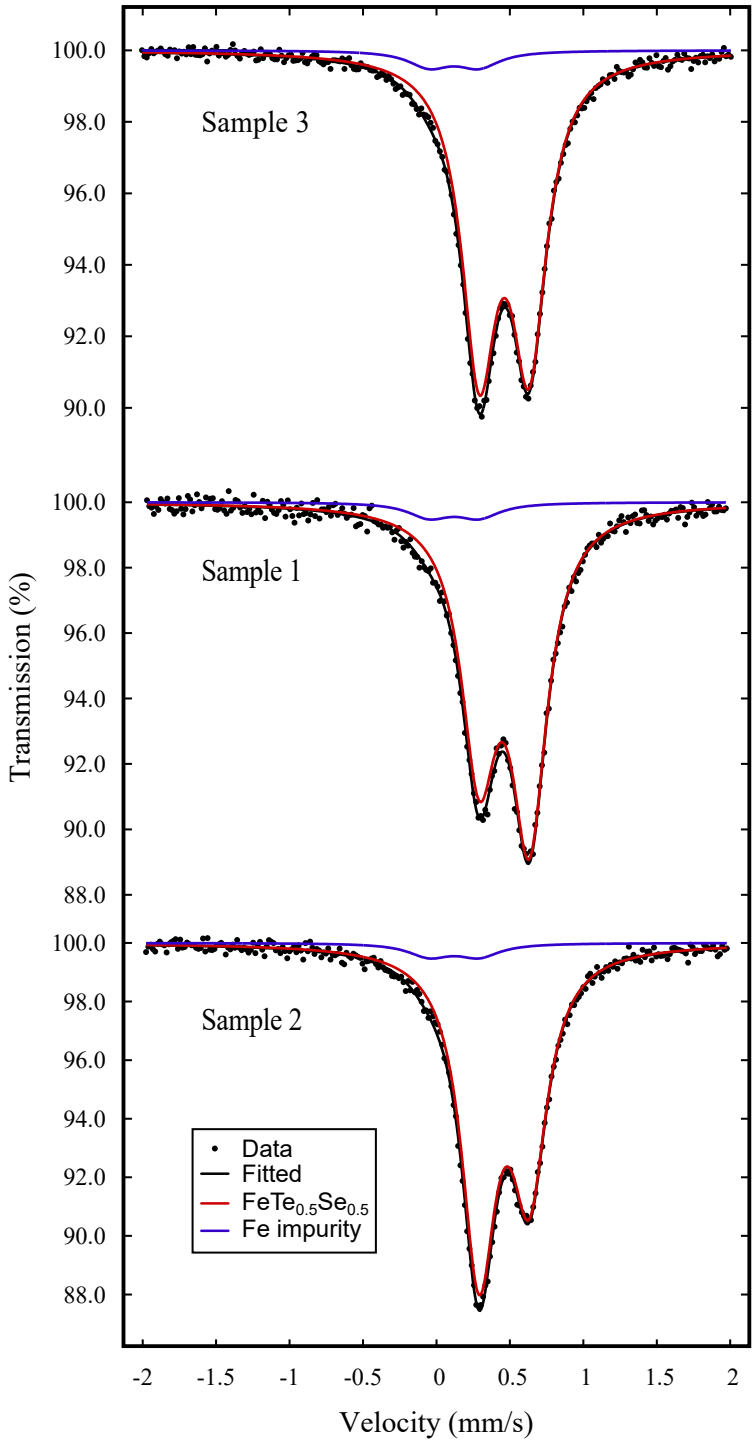

Figure 5.5: $FeTe_{0.5}Se_{0.5}$ Mössbauer spectra at 77.6 K for Sample 3 (turned $\sim 40°$), Sample 1 (exhibiting prominent $hk0$ peaks), and Sample 2 (exhibiting prominent $00l$ peaks). A small amount of Fe impurity in the detector window is seen as a weak symmetric doublet.

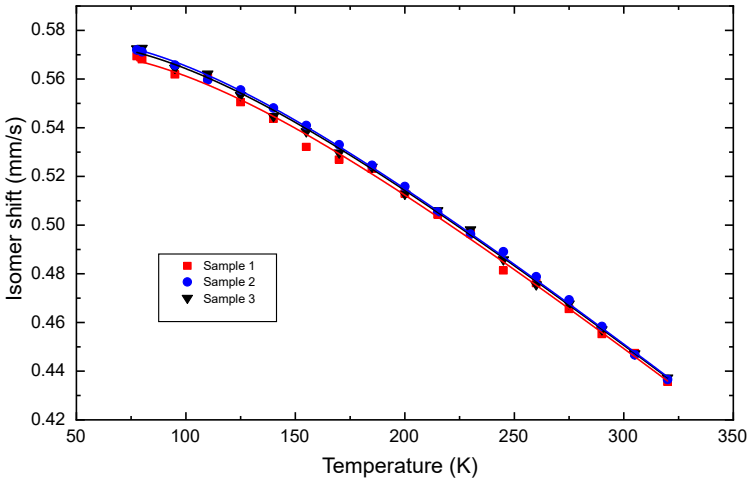

Figure 5.6: Isomer shifts vs. temperature fitted using the Debye model. Statistical errors do not exceed the size of the symbols.

of the temperature-dependent integrals of Eq. 2.15 and Eq. 2.7 differ so will the Debye temperatures, if the density of phonon states differs from the quadratic behavior of the Debye model. Nevertheless, a lattice anisotropy is observed for both the f_{a} factor and $\delta(T)$ confirming the presence of the GKE.

Using the distribution functions of the Rietveld analysis we can make an estimate of the θ_{ave} angles and compare them with those obtained from the Mössbauer data. Both texture effects and the GKE give rise to asymmetricity in the quadrupole doublet. For an axially symmetric case the angular-dependent gamma transition probabilities are proportional to $\frac{1}{4} + \frac{1}{4}\cos^2\theta_{\mathrm{ave}}$ and $\frac{1}{2}\sin^2\theta_{\mathrm{ave}}$ for transitions corresponding to $\Delta m = \pm 1$ and $\Delta m = 0$, respectively, as obtained from the relevant rotation matrix [39]. For a perfectly oriented sample measured in the so-called magic angle, $\theta_{\mathrm{ave}} = \arccos\frac{1}{\sqrt{3}}$, both factors yield $\frac{1}{3}$. The average texture angle θ_{ave} obtained from fitting the Mössbauer data can now be compared with the values obtained for the texture effects in the XRD patters by solving the following equation:

$$\frac{1}{4} + \frac{1}{4}\cos^2\theta_{\mathrm{ave}} = \int_0^{\frac{\pi}{2}} D(\theta)\left(\frac{1}{4} + \frac{1}{4}\cos^2\theta\right) f_{\mathrm{a}}(\theta)\sin\theta d\theta. \tag{5.4}$$

By entering the normalized distribution $D(\theta)$ from the Rietveld analysis and the likewise normalized $f_{\mathrm{a}}(\theta)$ function and performing a numerical integration we can obtain a value for θ_{ave} and compare it with the actual Mössbauer result obtained *e.g.* at 77 K. However, in order to do that we also need to calculate the f_{a} factors at 77 K using Eq. 2.15. The final result for θ_{ave} is: $71(1)^\circ$ and $39(1)^\circ$ for Samples 1 and 2, respectively. For Sample 1 there seems to be a systematic error of less than 10° compared to the angle obtained from the Mössbauer analysis. Possibly the model function for orientation in the Rietveld analysis is a bit crude. Furthermore, the X-rays probe only a thin surface layer, while the Mössbauer γ penetrates the whole sample.

CHAPTER VI

Mössbauer study of $Ba_2Ti_2Fe_2As_4O$

6.1 Motivation

In a vast class of iron-based superconductors, only very few are superconductors in their original stoichiometric composition of metals. Recently a new quinary oxypnictide $Ba_2Ti_2Fe_2As_4O$ with a superconducting transition temperature of $T_c \approx 21$ K was synthesized [40]. The compound $Ba_2Ti_2Fe_2As_4O$ belongs to the 22241 group of iron-based superconductors. The crystal structure of $Ba_2Ti_2Fe_2As_4O$ can be viewed as an intergrowth of $BaFe_2As_2$ [42] and $BaTi_2As_2O$ [43] containing superconducting [Fe_2As_2] layers and conducting [Ti_2O] sheets. Although neither $BaFe_2As_2$ nor $BaTi_2As_2O$ is superconducting, the combined structure shows superconductivity without doping. Based on the variation of bond-valence sum (BVS) of Ti [40, 45], electron transfer from Ti to Fe was proposed interpret the appearence of superconductivity as a result of self doping.

With this work we wanted to study the properties of the Fe atoms in $Ba_2Ti_2Fe_2As_4O$ using ^{57}Fe Mössbauer measurements.

6.2 Characterization of $Ba_2Ti_2Fe_2As_4O$

6.2.1 X-ray diffraction

Powder X-ray diffraction data used for the structural identification were collected at room temperature on an PanAnalytical X'Pert Pro MPD diffractometer using Cu $K\alpha 1$ radiation. Data were analyzed by the Rietveld method using the software program FullProf [33].

The tetragonal $I4/mmm$ space group was assumed for the main phase when analyzing the X-ray patterns of the $Ba_2Ti_2Fe_2As_4O$ X-ray samples. The pattern and the unit cell of $Ba_2Ti_2Fe_2As_4O$ Sample 1 are displayed in Fig. 6.1. All observed peaks can be indexed with reflections of the tetragonal main phase $Ba_2Ti_2Fe_2As_4O$ and the parent phase $BaFe_2As_2$. Possible signatures of the other parent phase $BaTi_2As_2O$ were close to or below the detection limit. The fitted values for the main-phase lattice parameters were $a = 4.022$ Å and $c = 27.298$ Å. The Rietveld refinement analysis [32] gave the volume percentages 87 and 13 for the main- and $BaFe_2As_2$ phases, respectively. For Sample 2 the Rietveld analysis yields the volume percentages of 92 and 8, respectively.

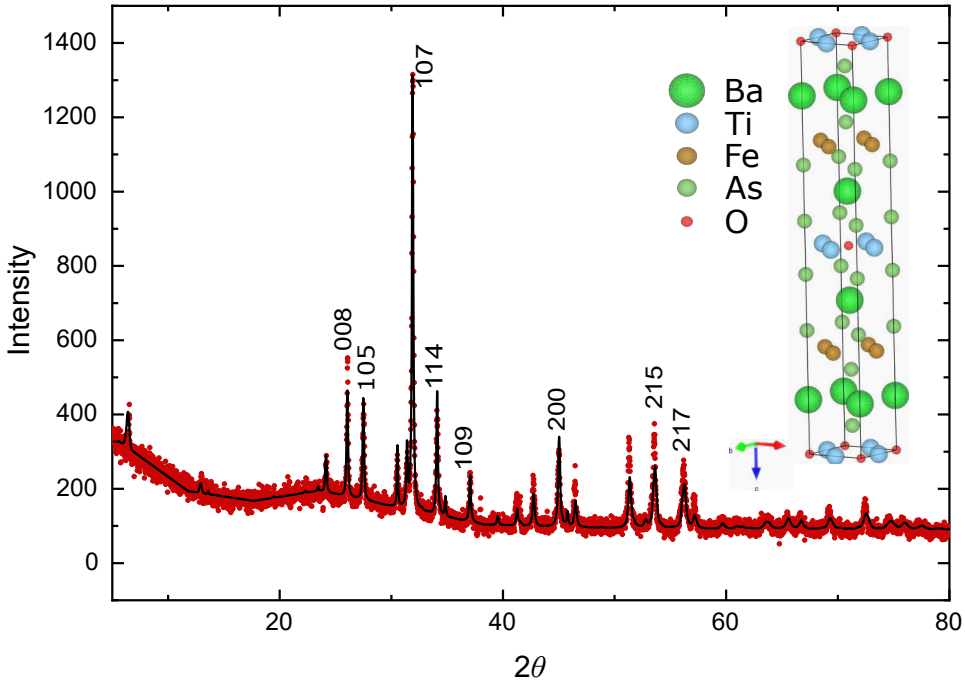

Figure 6.1: X-ray powder diffraction pattern for $Ba_2Ti_2Fe_2As_4O$ (Sample 1). Main reflections are indexed. Inset: structure of $Ba_2Ti_2Fe_2As_4O$.

6.2.2 Mössbauer spectra

For the Mössbauer measurements in transmission geometry both synthesised $Ba_2Ti_2Fe_2As_4O$ samples, Sample 1 as prepared and Sample 2 annealed at 773 K for 40 h in a vacuum, were reground and 50 mg of each powder was used for making the absorbers by mixing with an epoxy glue and spreading it evenly on a thin Al foil. The spectra were measured using a ^{57}Co:Rh source (Ritverc Co. 25mCi june 2018) with a maximum Doppler velocity of 2.55 mm/s and also controlled with Doppler velocity 10.00 mm/s for detection of magnetic phases. Measurements were done at several temperatures between 77 and 320 K. The samples were cooled using an Oxford CF506 continuous-flow cryostat with liquid N_2 as coolant. The temperature was controlled using an Oxford Intelligent Temperature Controller ITC 4. All spectra were fitted using the following Mössbauer parameters for the components: the magnetic hyperfine field B (when present), the quadrupole coupling constant eQV_{zz}, relative intensities, and isomer shift δ relative to α-Fe.

At 77 K the spectra of the Sample 1, Fig. 6.2 can be fitted using three components. The main component [red] of $Ba_2Ti_2Fe_2As_4O$ is paramagnetic and covers 77.5% of the spectral area at 77 K. A magnetically ordered component [green] covers 22.5% of the spectral area. It has a Néel temperature of ~ 140 K and comparing with the literature [41, 42] this seems to be $BaFe_2As_2$. At 77 K the two main components of both samples have almost equal isomer shifts values of ~ 0.58 mm/s and very small quadrupole splitting. The fitted value for the magnitude of the quadrupole coupling constant of $Ba_2Ti_2Fe_2As_4O$ at 77 K was $|eQV_{zz}| = 0.30(1)$ mm/s and 0.24(2) mm/s at room temperature. Additionally, there is a paramagnetic doublet [blue] covering a few percent of the spectral area. It is due to traces of Fe in the beryllium window of the detector and hence not included in the above calculation of total area. The parameters of that component were kept fixed during the fitting of all the Mössbauer data. For Sample 2 $Ba_2Ti_2Fe_2As_4O$ covers 65% and $BaFe_2As_2$ 35% of the spectral area at 77 K. The 77 K Mössbauer intensity portions are readily converted into mass proportions assuming perfect impurity stoichiometry and using the molar masses 797.78 g/mol for the main phase $Ba_2Ti_2Fe_2As_4O$, 398.87 g/mol for $BaFe_2As_2$, and 398.91 g/mol for the "invisible" $BaTi_2As_2O$ yielding mass portions of 78%, 11%, 11% and 65%, 17.6%, 17.5% for Samples 1 and 2, respectively, cf. also Eq. 7.1 for comparison.

Fe in $BaFe_2As_2$ and in the main phase have a practically identical local surroundings, *i.e.* a regular tetrahedron formed by four As neighbours, that gives rise to almost zero quadrupole splitting. As Fe orders magnetically in $BaFe_2As_2$, the spin state cannot be zero, but it is certainly no more than $S = 1$ [44]. When the sample is heated above the Néel temperature of $BaFe_2As_2$ the intensity of the component assigned to $Ba_2Ti_2Fe_2As_4O$ grows as the magnetic component due to $BaFe_2As_2$ disappears. Above 140 K the spin- and valence-dependent isomer shift values and absence of significant quadrupole splitting for the two main spectral components match perfectly. In $BaFe_2As_2$ Fe is formally divalent and it seems to be the case also for $Ba_2Ti_2Fe_2As_4O$. Therefore Ti is formally trivalent. In Fig. 6.4 and 6.3 the sum of the spectral absorption areas for the two main components in Samples 1 and 2 and the isomer shift for the main component are plotted as functions of the temperature. Owing to the fact that the component due to $Ba_2Ti_2Fe_2As_4O$ and the component due to $BaFe_2As_2$ merge upon passing the Néel temperature of the latter it is not possible separately obtain the absorption area nor the isomer-shift values for the main component above that temperature. Therefore, the absorption area for the sum of the two main components and the isomer-shift values of the main component, are given.
The isomer-shift data of Fig. 6.3 can be fitted using the Debye model for the second-order Doppler shift Eq. 2.7.

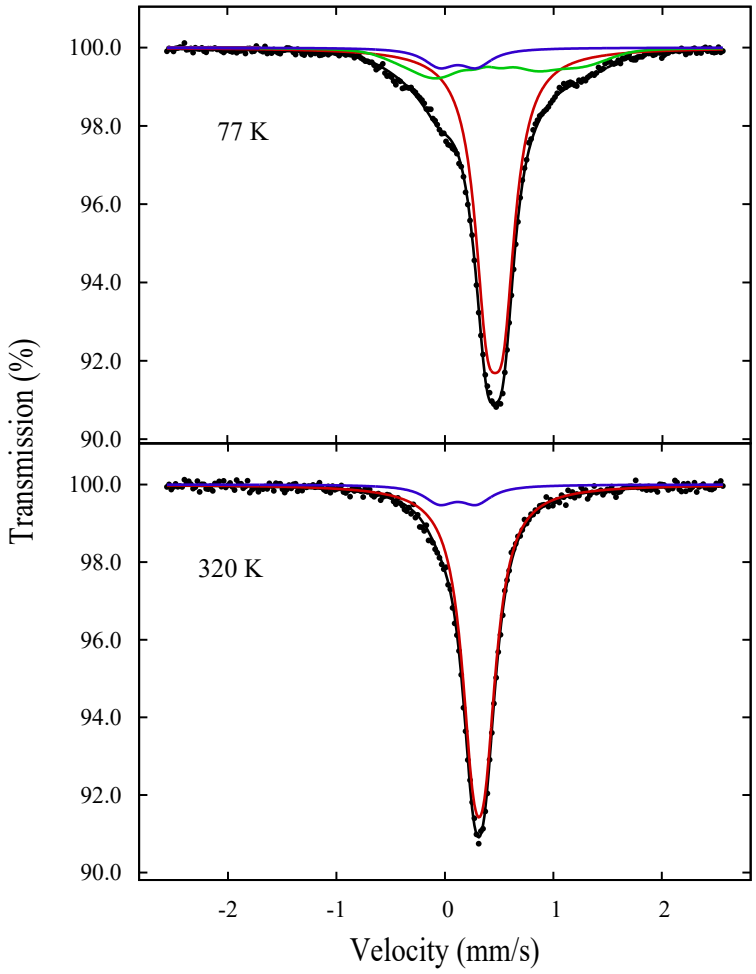

Figure 6.2: ^{57}Fe Mössbauer spectra of the $Ba_2Ti_2Fe_2As_4O$ (Sample 1) recorded at indicated temperatures. At 77 K the parent phase impurity $BaFe_2As_2$ gives rise to a magnetic sextet (green) that merges with the main phase (red) at 140 K. A weak doublet due to Fe in the detector window (blue) is present at all temperatures.

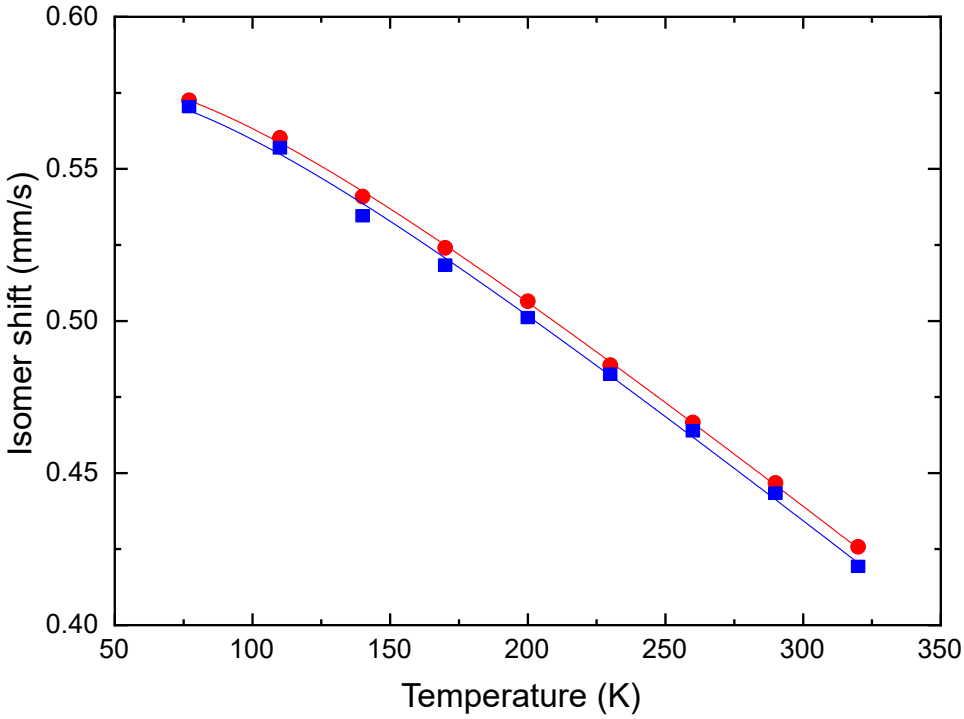

Figure 6.3: Isomer shift vs. temperature for $Ba_2Ti_2Fe_2As_4O$ Sample 1 (red bullets) and Sample 2 (blue squares). The data were fitted using the Debye model (see text) and the lines are the results of the fitting. Statistical errors do not exceed the size of the symbols.

Fitting the data yields $\delta_0 = 0.671(1)$ mm/s and $\delta_0 = 0.666(2)$ mm/s for Samples 1 and 2, respectively. The Debye-temperature values were fitted at $\theta_D = 326(8)$ K (Sample 1) and 316(17) K (Sample 2).

The total area of the spectrum is proportional to the recoil-free fraction f of absorption and can also be fitted using the Debye model Eq. 2.15.

In this case the fitted Debye temperatures were 305(4) K and 280(7) K for Samples 1 and 2, respectively.
In the Debye model a quadratic density of phonon states is assumed, which is necessarily not true in reality. As the integrals of Eq. 2.7 and Eq. 2.15 differ in the weighting of the normalized temperature $\frac{\theta_D}{T}$ the obtained Debye temperatures may differ considerably, which is not the case here. The density of phonon states cannot be obtained from the integrals, but the formal agreement between the two integrals suggests that the vibrations of the Fe atoms are fairly harmonic.

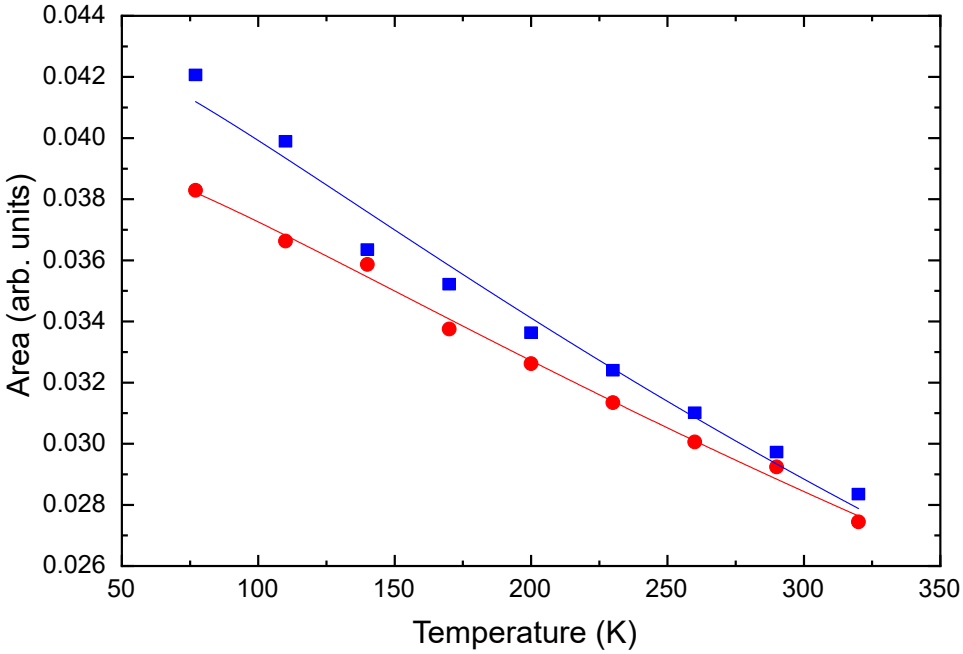

Figure 6.4: Total absorption area vs. temperature for $Ba_2Ti_2Fe_2As_4O$ Sample 1 (red bullets) and Sample 2 (blue squares). The data fitted using the Debye model (see text) and the lines are the results of the fitting. Statistical errors do not exceed the size of the symbols.

CHAPTER VII

Mössbauer study of $BaTh_2Fe_4As_4(N_{0.7}O_{0.3})_2$

7.1 Motivation

Recently, the first electron-doped double-Fe_2As_2-layer Fe-based superconductor, $BaTh_2Fe_4As_4(N_{0.7}O_{0.3})_2$ with $T_c^{onset} = 30$ K was discovered [46]. This 12442-type compound can be viewed as the result of intergrowth of (122-type) $BaFe_2As_2$ and (1111-type) $ThFeAsN_{0.7}O_{0.3}$. It was found that 12442-type iron-based superconductor was stabilized by the inter-block-layer charge transfer. This, inter-block-layer charge transfer, enhances the interlayer Coulomb attractions, which stabilizes the target phase. As the phase contains iron ^{57}Fe Mössbauer spectra can be used for recording presence of local magnetic- and electric interactions, as well to get information about the Fe valence and possible changes in the vibrational spectrum of Fe, which was the aim for this work.

7.2 Characterization of $BaTh_2Fe_4As_4(N_{0.7}O_{0.3})_2$

7.2.1 X-ray diffraction

Powder X-ray diffraction data used for the structural identification and analysis of phase composition were collected at room temperature on an PanAnalytical X'Pert Pro MPD diffractiometer using Cu $K\alpha 1$ (λ = 1.54051 Å) radiation. Data were analyzed by the Rietveld method [32] using the software program FullProf [33]. The tetragonal space group $I4/mmm$, No. 139, was used for $BaTh_2Fe_4As_4(N_{0.7}O_{0.3})_2$ to confirm the origin of the observed peaks in the diffraction pattern. The room-temperature powder X-ray diffraction pattern of the $BaTh_2Fe_4As_4(N_{0.7}O_{0.3})_2$ sample is displayed in Fig. 7.1. All observed peaks can be indexed with reflections of the main phase and the $ThFeAsN_{0.7}O_{0.3}$ impurity. The latter phase contains some oxygen judging by the value of lattice parameter $a = 3.98659$Å [48]. The fitted lattice parameter values for the $BaTh_2Fe_4As_4(N_{0.7}O_{0.3})_2$ were $a = 3.9886$ Å and $c = 29.853$ Å. The Rietveld refinement analysis of the XRD spectrum gave the weight percentages for the main component $BaTh_2Fe_4As_4(N_{0.7}O_{0.3})_2$ 88.24 and for $ThFeAsN_{0.7}O_{0.3}$ 11.76, respectively. Assuming perfect interelemental stoichiometry the Rietveld result can be converted into Fe mass portions using the molar mass and iron mass percent for each component. Although $BaFe_2As_2$ is "invisible" (due to the detection limit for for XRD of $\approx 5\%$) in the Rietveld analysis, the following sample composition is assumed:

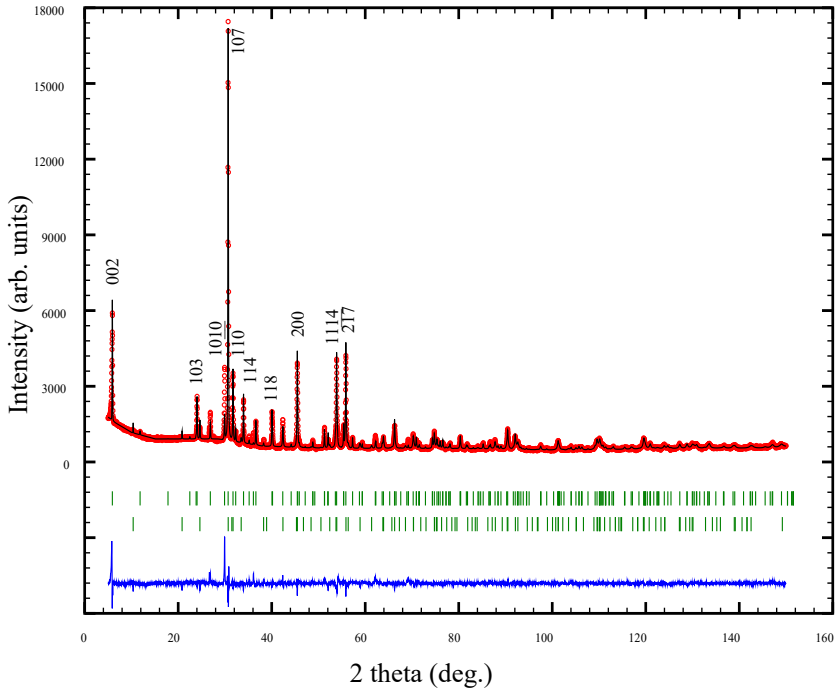

Figure 7.1: X-ray powder diffraction pattern for $BaTh_2Fe_4As_4(N_{0.7}O_{0.3})_2$. Main reflections are indexed.

$$[ThFeAsN_{0.7}O_{0.3}]_{2x} + [BaFe_2As_2]_x + [BaTh_2Fe_4As_4(N_{0.7}O_{0.3})_2]_{1-x}, \tag{7.1}$$

where x denotes the concentration of impurities.
The conversion is based on the molar masses of the three phases: 376.81, 398.86, and 1153.68 g/mol, for $ThFeAsN_{0.7}O_{0.3}$, $BaFe_2As_2$, and $BaTh_2Fe_4As_4(N_{0.7}O_{0.3})_2$ respectively. The corresponding mass percentages of Fe are 14.82, 28.00, and 19.36 in the three phases, respectively. Based on this we expect that 4.04%, 7.65%, and 88.31% of the signal in the Mössbauer measurements to arise from the three phases $ThFeAsN_{0.7}O_{0.3}$, $BaFe_2As_2$ and $BaTh_2Fe_4As_4(N_{0.7}O_{0.3})_2$ respectively.

7.2.2 Mössbauer spectra

For the Mössbauer measurements in transmission geometry the sample was reground and 80 mg of the powder was used for making the absorber by mixing with an epoxy glue and spreading it evenly on a thin Al foil. The spectra were measured using ^{57}Co:Rh source (Ritverc Co. 50 mCi June 2020) at temperatures between 4.8 K and 305 K using maximum Doppler velocities of 2.0 and 2.6 mm/s. Additional control with a Doppler velocity $\sim$ 10 mm/s for detection of magnetic phases was done. The sample was cooled using the Oxford CF 506 continuous-flow cryostat with liquid helium between 4,8$-$150 K and with liquid nitrogen between 77 K and 305 K. At the start of the low-temperature measurements the test chamber was partly filled with helium gas to ensure

proper thermal conduct to the sample. The temperature was controlled using an Oxford Intelligent Temperature Controller ITC 4. All spectra were fitted using a home-written program with the following Mössbauer parameters for the components: the quadrupole coupling constant eQV_{zz}, relative intensities, isomer shift δ relative to α-Fe and internal hyperfine magnetic field B when present. Transmission integral fitting with the MossWinn 4.0 program [34] of selected spectra were used to confirm that the samples could be regarded as thin and that the line shape exhibits a small quadrupole splitting.

At all temperatures the ^{57}Fe Mössbauer spectra are dominated by a singlet-like resonance line of the sample, (see Fig. 7.2). They can be fitted using one to two components in addition to the main singlet drawn in red. Absence of magnetic interaction for the dominating component indicates that possible spin-density wave magnetism is suppressed down to 5 K. According to the literature [47], ThFeAsN gives rise to a singlet-like line, seemingly identical to the main phase-component we observe, and consequently they are indistinguishable from each other. While the Rietveld analysis revealed only two phases $BaTh_2Fe_4As_4(N_{0.7}O_{0.3})_2$ and $ThFeAsN_{0.7}O_{0.3}$, in the Mössbauer data we also see at temperatures below ~ 140 K indications of weak magnetic structures assigned to $BaFe_2As_2$ (drawn in black in Fig. 7.2). At room-temperature $BaFe_2As_2$ gives rise to a singlet and orders magnetically at ~ 140 K [42]. Hence, above 140 K the two parent phases and the main phase are indistinguishable using Mössbauer spectroscopy [49]. Additionally, a small paramagnetic doublet (green), due to traces of Fe in the beryllium window of the detector, present at all temperatures is included in the fittings, but omitted from the calculation of the spectral area. The parameters of this component were kept fixed during the fittings of all the Mössbauer data.

The appearance of a small quadrupole splitting at lower temperatures indicates a slight deformation of the tetrahedral As coordination around the Fe atoms. This is in accord with the analysis of X-ray diffraction data [46]. However, in the Mössbauer data the deformation becomes visible only below 80 K. Above 80 K the quadrupole splitting may remain below the detection limit, as the quadrupole coupling constant usually increases with decreasing temperature, as e.g. in the ThFeAsN phase [47].

Fe atoms in $ThFeAsN_{0.7}O_{0.3}$, $BaFe_2As_2$ and in $BaTh_2Fe_4As_4(N_{0.7}O_{0.3})_2$ have practically identical local surroundings, $i.e.$ a regular or almost regular tetrahedron formed by four As neighbours, that gives rise to almost zero quadrupole splitting. This is in accord with the single-like feature observed. Initially the first Mössbauer spectra were fitted using the singlet and the paramagnetic doublet only. At temperatures below 80 K releasing non-zero values for the quadrupole interaction improved the fitting of the "singlet". Also transmission-integral fittings using the program MossWin gave a non-zero quadrupole splitting at these temperatures. Some concern was raised concerning whether the omission of a weak magnetic component could cause the emergence of a non-zero eQV_{zz}, which is why we decided to fit the spectra both with and without the almost invisible phase $BaFe_2As_2$. Including the phase slightly improved the fitting, but most importantly non-zero eQV_{zz} values were obtained for the main phase using both fitting schemes. The fitted values for eQV_{zz} are shown in Fig. 7.3. Certain parameter fixing and/or limitations had to be imposed on the magnetic sextet of $BaFe_2As_2$. The isomer shift was constrained equal to that of the main singlet. The internal field was constrained to be ≥ 3.8 T and for the quadrupole interaction we constrained $|eQV_{zz} < 0.3|$ mm/s. Finally, the intensity was constrained to be $\leq 5.0\%$. Below 25 K non of these constrains were actually needed, but at higher temperatures some of them were. Owing to the fact that the main component and the parent component $ThFeAsN_{0.7}O_{0.3}$ merge at all temperatures and the component due to $BaFe_2As_2$ also merges upon passing its Néel temperature it is not possible separately to obtain the absorption area nor the isomer shift values for the main component. Therefore, the total

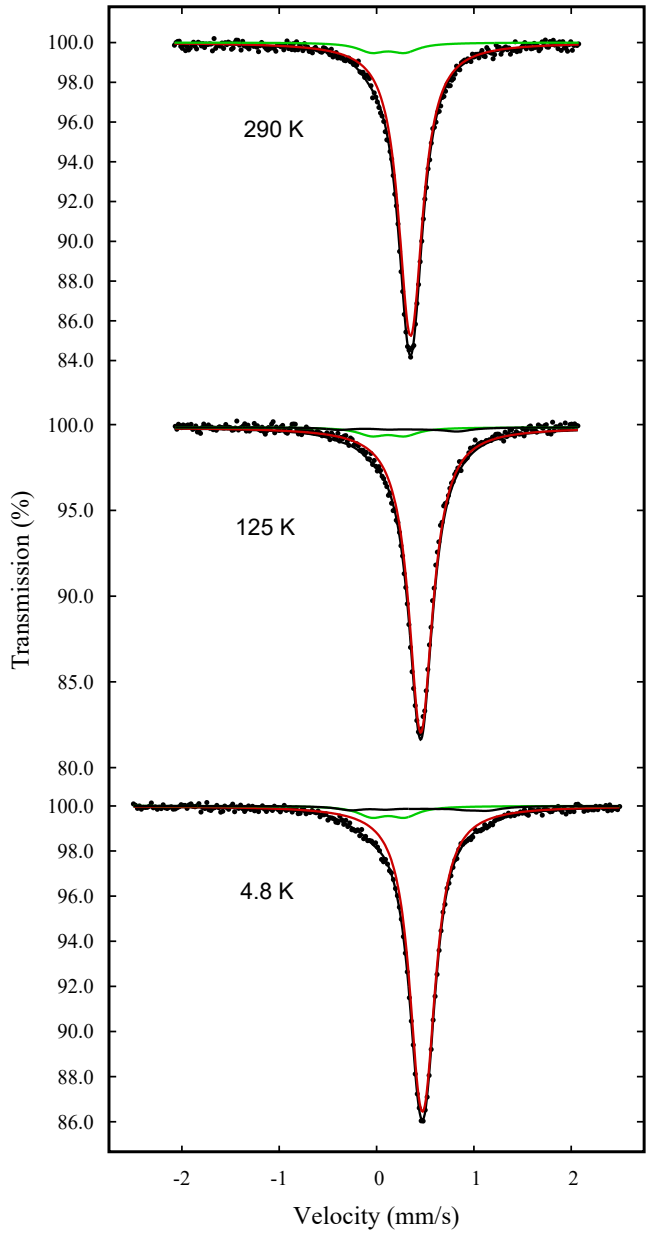

Figure 7.2: ^{57}Fe Mössbauer spectra of $BaTh_2Fe_4As_4(N_{0.7}O_{0.3})_2$ recorded at indicated temperatures. The spectra is dominated by the singlet-like line due to the main phase (red). At low temperatures parent phase $BaFe_2As_2$ gives rise to a small magnetic sextet (black) that merges with the main phase at 140 K. ThFeAsN cannot be distinguished from the main phase at any temperature. A weak doublet due to Fe in the detector window (green) is present at all temperatures.

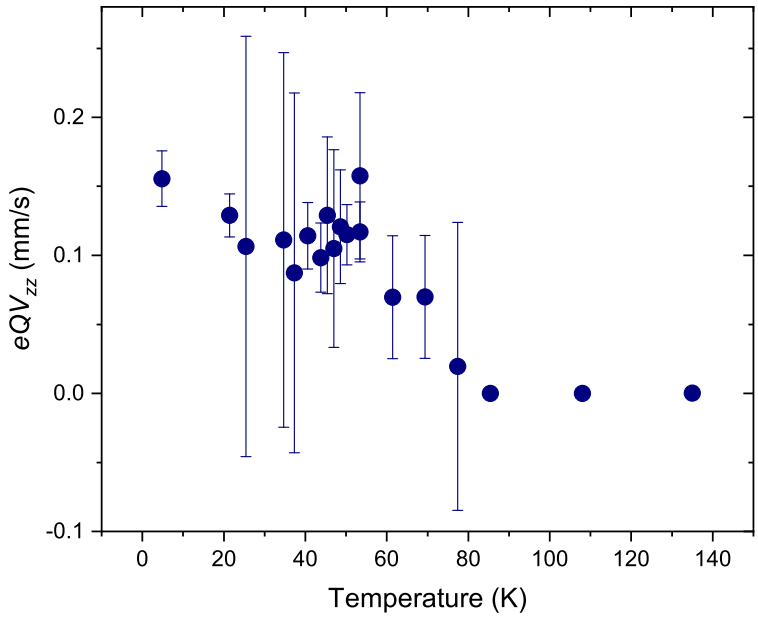

Figure 7.3: Experimentally obtained values for eQV_{zz} of $BaTh_2Fe_4As_4(N_{0.7}O_{0.3})_2$ below 140 K.

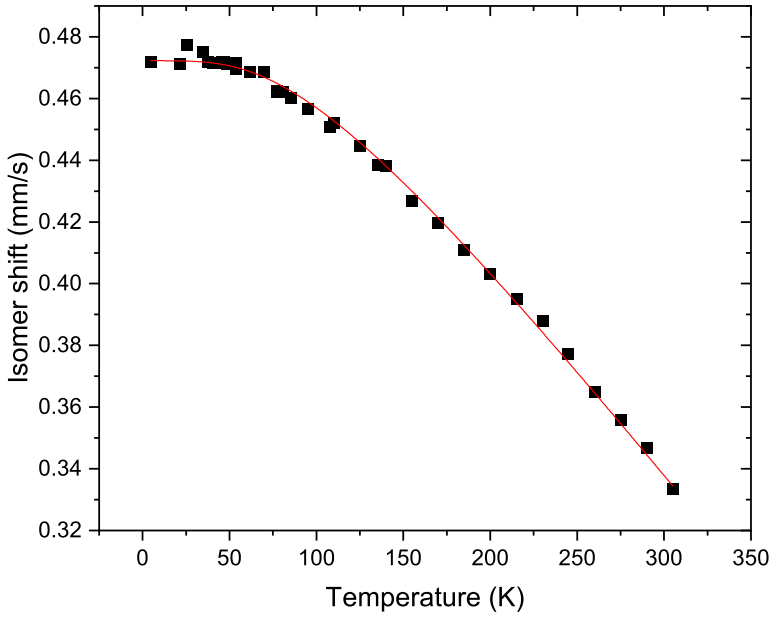

Figure 7.4: Isomer shift vs. temperature for $BaTh_2Fe_4As_4(N_{0.7}O_{0.3})_2$. The data was fitted using the Debye model (see text) and the line is the result of the fitting without α-Fe correction. Statistical errors do not exceed the size of the symbols.

absorption area for the whole spectrum, except that of the detector window, and the isomer shift values of the main component are presented in Fig. 7.4 and 7.5 as functions of the temperature.

The isomer-shift data of Fig. 7.4 can be fitted using the Debye model [38] for the second-order Doppler shift Eq. 2.7. Fitting the data yields δ_0 = 0.573(1) mm/s, which is compatible with low-spin Fe^{2+}. The isomer-shift data of $Ba_2Ti_2Fe_2As_4O$ and $BaTh_2Fe_4As_4(N_{0.7}O_{0.3})_2$ are virtually identical as they have practically the same environment around Fe. The Debye-temperature value was fitted at θ_D = 369(5)K.

The total area of the spectra of Fig. 7.5 is proportional to the recoil-free fraction f of absorption and can also be fitted using the Debye model [37] for the energy distribution of phonons in Eq. 2.15 where the recoil energy E_R = 0.0019 eV for the 14.4 keV γ quantum of ^{57}Fe. In this case the fitted Debye temperature was 352(5) K. In the Debye model a quadratic density of phonon states is assumed, which is necessarily not true in reality. As the integrals of Eg. 2.7 and Eq. 2.15 differ in the weighting of the normalized temperature $\frac{\theta_D}{T}$, the obtained Debye temperatures may differ considerably, which is not the case here. This indicates that the vibrations of the Fe atoms are fairly harmonic.

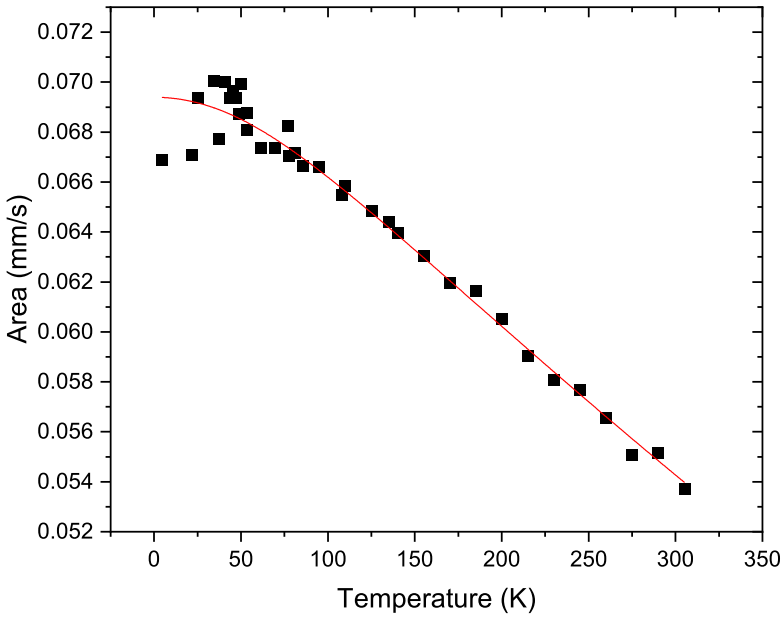

Figure 7.5: Total absorption area vs. temperature for $BaTh_2Fe_4As_4(N_{0.7}O_{0.3})_2$. The data was fitted using the Debye model and the line is result of the fitting. Statistical errors do not exceed the size of the symbols.

CHAPTER VIII

Conclusions

A slightly non-stoichiometric monoclinic Fe_3Se_4 sample with a selenium content of 56.1 at% was successfully synthesized by a solid-state reaction method. Power X-ray diffraction data used for phase identification were collected at room temperature and Rietveld analysis was used to confirm the origin of the observed peaks in the diffraction pattern. The magnetic properties of the Fe_3Se_4 sample were characterized using ^{57}Mössbauer spectroscopy in transmission geometry at various temperatures between 77 and 360 K. The two iron sites were readily identified from the two magnetic sextets observed below Curie temperature $T_C \approx 331$ K. Using only two simple sextets with no distributions yielded poor fittings. Both sextets exhibit sign of broadening, neither the high- nor the low-field part could be completely explained by one component each. This could be dealt with, either by doubling the number of sextets to four, or by introducing a correlated histogram distribution to each sextet. However using four-component fitting one of the low-field components exhibited excessive broadening, which is curious as it should originate from the same iron site as the other low-field component, which did not exhibit broadening. To analyse the internal hyperfine field by helical magnetism gave no result. It is inferred that the origin of the distribution is a charge-distribution occurring within each iron site.
The best result was obtained using only two components with hyperfine parameter distributions released. At T_C the distributions narrow down, but remain still considerable in particular for iron at lattice site 1 up to at least 360 K - the highest temperature reached in this work. The internal fields for the iron atoms are low. For both sites the average field is considerably below the expected high-spin values, which is interpreted as an intermediate-spin state, with additional anti-parallel contributions from the dipolar field of the doubly-occupied d orbital, which is in accord with the large quadrupole coupling constant observed.
Our non-stoichiometric $FeSe_{1.2779}$ sample was later studied by Girish C Tewari et.al and possible signatures of half metallicity were found [54],

A solid-state reaction scheme was used for the synthesis of the iron chalcogenide sample with nominal composition $FeTe_{0.5}Se_{0.5}$. Two samples were texturized using an external magnetic field. As the main axis is inclined to orient perpendicular to the field a special device is needed for obtaining preferentially aligned c axes. For this purpose a Bruker Ultra-High-Field NMR magnet 11.7 T was used together with a self-constructed gearbox mechanism which allowed the sample to be magnetized both in $\parallel$ or in $\perp$ position in the 11.7 T field. The phase and structure determination of the as-synthesized powder and the magnetically aligned absorbers were carried out at room tempera-

ture with a X-ray powder diffractometer. Data were analysed by the Rietveld method in the FullProf program.
By using Mössbauer absorbers with three differing textures; close to random orientation, c axes predominantly parallel with, and predominantly perpendicular to the $\mathbf{k}_\gamma$ vector, we were able to show that the recoil-free fraction of absorption has a small lattice anisotropy, i.e. $FeTe_{0.5}Se_{0.5}$ exhibits the Goldanskii-Karyagin effect. The estimated 0 K value for the f_a factor was 0.907 along the c axis and 0.851 perpendicular to it. The lattice anisotropy is also observed in the Rietveld analysis of the atomic displacement parameters of iron, with the largest displacement parameter obtained along the c axis direction and smallest along the ab plane in agreement with the results from the analysis of the Mössbauer spectra. Experiments like this enables reliable dedection of the sign and V_{zz} and of course the GKE.

Polycrystalline oxypnictide $Ba_2Ti_2Fe_2As_4O$ can be viewed as an intergrowth of $BaFe_2As_2$ and $BaTi_2As_2O$ containing superconducting [Fe_2As_2] layers and conducting [Ti_2O] sheets. Although neither $BaFe_2As_2$ nor $BaTi_2As_2O$ is superconducting, the combined structure shows superconductivity without doping. $Ba_2Ti_2Fe_2As_4O$ is subjected to an effective self-douping property.
^{57}Fe Mössbauer spectra of the oxypnictide $Ba_2Ti_2Fe_2As_4O$ indicate that the SDW magnetism is suppressed at least down to 77 K, while for the parent phase $BaFe_2As_2$ it is present up to ~ 140 K. Above 140 K the electric hyperfine parameters of $BaFe_2As_2$ and $Ba_2Ti_2Fe_2As_4O$ are practically identical, with a very small quadrupole splitting of $eQV_{zz}/2 \approx 0.15(1)$ mm/s which is accordance with the rather symmetric As coordination of Fe. Using the Debye model for analyzing the temperature-dependent part [SOD] of the isomer shift data and the sample absorption for $Ba_2Ti_2Fe_2As_4O$, a Debye temperature of 280-320 K is obtained. The temperatures are rather low, indicating that the local lattice around Fe is rather soft. The chemical isomer shift value indicates that Fe is formally divalent with a low spin. As Fe orders magnetically in $BaFe_2As_2$, the spin state is probably close to $S = 1$. The fact that there is no detectable difference in the isomer shift values for $Ba_2Ti_2Fe_2As_4O$ and $BaFe_2As_2$ indicates that there is no charge transfer to the Fe atom when the ordered structure containing titanium forms. Measurements below 77 K might shed more light on the difference between and similarities of the parent phase and the superconductive one.

Recently the first electron-doped double-Fe_2As_2-layer Fe-based superconductor,
$BaTh_2Fe_4As_4(N_{0.7}O_{0.3})_2$ with T_c^{onset} = 30 K was synthesized. At all temperatures the ^{57}Fe Mössbauer spectra are dominated by a singlet-like resonance line of the sample, Fig. 7.2. Absence of magnetic interaction for the dominating component indicates that possible spin-density wave magnetism is suppressed down to 5 K. Using the Debye model for analyzing the temperature-dependent part of the isomer shift data and the sample absorption, yields Debye temperatures of 352-369 K, which are similar to those obtained for other pnictide superconductors. In the Debye model a quadratic density of phonon states is assumed, which is necessarily not true in reality. As the integrals of Eq. 2.7 and Eq. 2.15 differ in the weighting of the normalized temperature $\frac{\theta_D}{T}$ the obtained Debye temperatures may differ considerably, which is not the case here. This indicates that the vibrations of the Fe atoms are fairly harmonic. The chemical isomer shift value indicates that the Fe is divalent in low-spin state when Th valence is close to +4 and As valence close to -3. A nonzero quadrupole splitting is seen below 80 K, reflecting the deviation from the regular tetrahedral coordination of As around Fe.

[1] H. Okamoto, The Fe-Se (Iron-Selenium) System, Journal of Phase Equilibria 12 (1991) 383-384.

[2] F.-Ch. Hsu, J.-Y. Luo, K.-W. Yeh, T.-K. Chen, T.-W. Huang, Ph. M. Wu, Y.-Ch. Lee, Y.-L. Huang, Y.-Y. Chu, D.-Ch. Yan, and M.-K. Wu, Proc. Natl. Acad. Sci. U.S.A. 105 (2008) 14262.

[3] C. N. R. Rao, B. Raveau, *Transition Metal Oxides*, 2nd Ed. (Wiley, 1995) p. 325.

[4] C. Boumford, A.H Morrish, Physica Status Solidi (A) 22 (1974) 435.

[5] B. Lambert-Andron and G. Berdias, Solid State Communications, 7 (1969) 623-629.

[6] A. Sklyarova, J. Lindén, G.C. Tewari, E.-L. Rautama, and M. Karppinen, Hyp. Int. 226 (2014) 341-349.

[7] J.R. Régnard and J.C. Hocquenghem, J. Phys. Colloques, 32 (1971) C1-268-270.

[8] C. Pak, S. Kamali, J. Pham, K. Lee, Joshua T. Greenfield, and K. Kovnir, J. Am. Chem. Soc., 135 (2013), 19111-19114.

[9] A.F. Andresen, Acta Chem. Scand. 22 (1968) 827-835.

[10] A.F . Andresen and B. van Laar, Acta Chem. Scand. 24 (1970) 2435-2439.

[11] B. Lambert-Andron, G. Berdias, and D. Babot, J. Phys. Chem. Solids 33 (1972) 87-94.

[12] S. Li, S.F. Lin, J. Ji, Z.N. Guo, and W.X. Yuan, Powder Diffraction 28 (2013) S32-S36.

[13] N.N. Greenwood, T.C. Gibb, in *Mössbauer Spectroscopy, 1st ed.* (Chapman and Hall, London 1971) p. 87.

[14] M.S. Bishwas, R. Das, and P. Poddar, The Journal of Physical Chemistry C, 118 (2014) 4016-4022.

[15] I.S. Lyubutin, Chun-Rong Lin, K.O. Funtov, T.V Dimitrieva, S.S. Starchikov, Yu-Jhan Siao, and Mei-Li Chen, The Journal of Chemical Physics, 141 (2014) 044704-10.

[16] N.N. Greenwood, T.C. Gibb, in *Mössbauer Spectroscopy, 1st ed.* (Chapman and Hall, London 1971) p. 93.

[17] J. Lindén, F. Lindroos, and P. Karen, J. Solid State Chem. 252 (2017) 119-128.

[18] N.N. Greenwood, T.C. Gibb, in *Mössbauer Spectroscopy, 1st ed.* (Chapman and Hall, London 1971) pp. 50-53.

[19] V.I. Goldanskii, Mössbauer effect in tin compounds. Proc. Acad. Sci. USSR (Phys. Chem. Sect.) 147 (1962) 766-768.

[20] Herber, R.H.: *Structure, bonding and the Mössbauer lattice temperature.* In: Herber, R.H. (ed.) Chemical Mössbauer Spectroscopy. (Plenium, New York 1984).

[21] N.N. Greenwood, T.C. Gibb, in *Mössbauer Spectroscopy, 1st ed.* (Chapman and Hall, London 1971) pp. 74-76.

[22] Alexey V. Sobolev, Igor A. Presniakov, Andrey A. Gippius, Ivan V Chernyavskii, Martina Schaedler, Norbert Buettgen, Sergey a. Ibragimov, Igor V. Morozov, Andrey V. Shevelkov, Helical magnetic structure and hyperfine interactions in FeP studied by ^{57}Fe Mössbauer spectroscopy and ^{31}P NMR, Journal of Alloys and Compounds 675 (2016) 277-285.

[23] S. V. Karyagin, A possible cause for the doublet component asymmetry in the Mössbauer absorpption spectrum of some powdered tin compounds, Proc. Acad. Sci. USSR (Phys. Chem. Sect.)148 (1963) 110-112.

[24] Adam Sobkowiak, Kristina Edström, Tore Ericsson and Torbjörn Gustafsson, A Mössbauer spectroscopy studyd of polyol synthesized tavorite $LiFeSO_4F$, Hyperfine Interact, DOI 10.1007/s10751-013-0935-1.

[25] R. M. Sternheimer, Shielding and Antishielding of Nuclear Quadrupole Moments, Z. Naturforsch. 41 a (1986) 24-36.

[26] M.H. Fang, H.M. Pham, B. Qian, T.J. Liu, E.K. Vehstedt, Y. Liu, L. Spinu, and Z.Q. Mao, Phys. Rev. B 78 (2008) 224503.

[27] K. Szymański, W. Olszewski, L. Dobrzyński, D. Satuła, D.J. Gawryluk, M. Berkowski, R. Puźniak, and A. Wiśniewski, Supercond. Sci. Technol. 24 (2011) 105010.

[28] J. Lindén, M. Lippmaa, T. Karlemo, M. Karppinen, and L. Niinistö, Supercond. Sci. Technol. 9 (1996) 399.

[29] N.N. Greenwood and T.C. Gibb, in *Mössbauer Spectroscopy*, 1st ed. (Chapman and Hall, London 1971), p. 74.

[30] U. Gonser and H.-D. Pfannes J. de Physique, 35 (1974) C6-113.

[31] A. Sklyarova, J. Lindén, G. C. Tewari, E.-L. Rautama, M. Karppinen, Hyperfine Interact 226 (2014) 341.

[32] H.M. Rietveld, Acta Cryst. 22, 151, (1967).

[33] J. Rodriguez-Carvajal, Physica B 192 (1993) 55.

[34] Homepage of MossWinn 4.0 program www.mosswinn.com, accessed February 2020.

[35] K.J.S. Silva, D.A.L. Tellez, C.A.P. Vargas, D.M. Buitrago, C.A.C. Passos, I.M. Capucho, J.N.O. Pinto, V.T. Abílio, and J.A. Aguiar, J. Supercond. Nov. Magn. 30 (2017) 1699.

[36] N.N. Greenwood and T.C. Gibb, in *Mössbauer Spectroscopy*, 1st ed. (Chapman and Hall, London 1971), p. 13.

[37] G. Schatz and A. Weidinger in *Nuclear Condensed Matter Physics: Nuclear Methods and Applications* (Wiley, Chichester 1996), p. 41.

[38] F. Menil, J. Phys. Chem. Solid. 46 (1985) 763.

[39] M.E. Rose, in *Elementary Theory of Angular Momentum*, 1st ed. (Wiley, New York 1957), p. 67.

[40] Yun-Lei Sun, Hao Jiang, Hui-Fei Zhai, Jin-Ke Bao, Wen-He Jiao, Qian Tao, Chen-Yi Shen, Yue-Wu Zeng, Zhu-An Xu, and Guang-Han Cao, J. Am. Chem. Soc. 134 (2012) 12893-12895.

[41] A.S. Sefat, L. Li, H.B. Cao, M.A. McGuire, B. Sales, R. Custelcean, ans D.S.Parker, Phys. Rev. Lett. 101 (2088) 117004.

[42] Marianne Rotter, Marcus Tegel, and Dirk Johrendt, Phys. Rev. Lett. 101 (2008) 107006.

[43] C. Wang, Z. C. Wang, Y. X. Mei, Y. K. Li, L. Li, Z. T. Tang, Y. Liy, P. Zhang, H. F. Zhai, Z. A. Xu andG. H. Cao, J. Am. Chem. Soc., 138 (2016) 2170.

[44] A. Błachowski, K. Ruebenbauer, J. Żukrowski, and Z. Bukowski, Journal of Alloys and Compounds 582 (2014) 167.

[45] Hao Jiang, Yun-Lei Sun, Jianhui Dai, Guang-Han Cao, and Chao Cao, PACS numbers: 74.70.Xa; 71.20.Ps; 75.30.Fv; 74.20.Pq.

[46] Y-T. Shao, Z-C Wang, B-Z. Li, S-Q. Wu, J-F. Wu, Z. Ren, S-W. Qiu, C. Rao, C. Wang and G-H. Cao, Science China Materials, 62 (2019) 1357.

[47] M. A. Albedah, F. Nejadsattari, Z. Stadnik, Zhi-Cheng Wang, Cao Wang, Guang-Han Cao, J. Alloys Comp., 695 (2017) 1128.

[48] Bai-Zhuo Li, Zhi-Cheng Wang, Jia-Lu Wang, Fu-Xiang Zhang, Dong-Ze Wang, Feng-Yuan Zhang, Yu-Ping Sun, Qiang Jing, Hua-Fu Zhang, Shu-Gang Tang, Yu-Ke Li, Chun-Mu Feng, Yu-Xue Mei, Cao Wang and Guang-Han Cao, J. Phys. Cond Matter. 30 (2018) 255602.

[49] R. Pohjonen, J. Lindén, Shi-Huai Sun, and Guang-Han Sun, J. Alloys Comp., 848 (2020) 155706.

[50] LeBail A. Powder Diffraction, 20 (2005) 316-326.

[51] An introduction to the program FullProf 2000 (Version July 2001), Juan Rodriquez-Carvajal.

[52] Harold Klug and Leroy Alexander, *X-ray diffraction procedures for polycrystalline and amorphous materials* (Wiley, 2nd ed. 1973) p.167

[53] N.N. Greenwood and T.C. Gibb, in *Mössbauer Spectroscopy*, 1st ed. (Chapman and Hall, London 1971), pp. 12-13.

[54] Girish C Tewari, Divya Srivastava, Reijo Pohjonen, Otto Mustonen, Antti J Karttunen, Johan Lindén and Maarit Karppinen, J.Phys.: Condens. Matter. 32 (2020) 455801.

[55] N.N. Greenwood, T.C. Gibb, in *Mössbauer Spectroscopy, 1st ed.* (Chapman and Hall, London 1971) p. 10.

[56] N.N. Greenwood, T.C. Gibb, in *Mössbauer Spectroscopy, 1st ed.* (Chapman and Hall, London 1971) p. 56.

[57] N.N. Greenwood, T.C. Gibb, in *Mössbauer Spectroscopy, 1st ed.* (Chapman and Hall, London 1971) p. 60.

[58] Hiroki Takahashi, Nature, 453 (2008) 376-378

[59] N.N. Greenwood, T.C. Gibb, in *Mössbauer Spectroscopy, 1st ed.* (Chapman and Hall, London 1971) p. 50.

[60] N.N. Greenwood, T.C. Gibb, in *Mössbauer Spectroscopy, 1st ed.* (Chapman and Hall, London 1971) p. 52.

[61] N.N. Greenwood, T.C. Gibb, in *Mössbauer Spectroscopy, 1st ed.* (Chapman and Hall, London 1971) p. 63.

[62] N.N. Greenwood, T.C. Gibb, in *Mössbauer Spectroscopy, 1st ed.* (Chapman and Hall, London 1971) p. 55

[63] Philip R. Bevington, D. Keith Robinson, *Data Reduction and Error Analysis for the Physical Sciences, 3rd ed.* (McGraw-Hill, New York 2003) pp.102-114

[64] Yi Liu, Ya-Bin Liu, Qian Chen, Zhang-Tu Tang, Wen-He Jiao, Qian Tao, Zhu-An Xu and Guang-Han Cao, A new ferromagnetic superconductor: $CsEuFe_4As_4$, Science Bulletin (2016), DOI:10.1007/s11434-016-1139-2

[65] Hiroyoshi Nobukane , Kosei Yanagihara, Yuji Kunisada, Yunito Ogasawara, Kakeru Isono, Kazushige Nomura, Keita Tanahashi, Takahiro Nomura, Tomohiro Akiyama and Satoshi Tanda, Co-appearance of superconductivity and ferromagnetism in a Ca_2RuO_4 nanofilm crystal, Scientific Reports (2020)10:3462 https://doi.org/10.1038/s41598-20-60313-x

[66] Terry A. Ring, *Fundamentals of Ceramic Powder Processing and Synthesis* (Academic Press 1996) pp.81-83, 139-178, 777-780.

ISBN 978-952-12-4163-5